Technological University Dublin
ARROW@TU Dublin

Masters | Science

2004-01-01

High-speed Electronic Speckle Pattern Interferometry

Carol Armstrong
Technological University Dublin

Follow this and additional works at: https://arrow.tudublin.ie/scienmas

Part of the Physics Commons

Recommended Citation

Armstrong, C. (2004). *High-speed electronic speckle pattern interferometry*. Masters dissertation. Technological University Dublin. doi:10.21427/D7MK79

This Article is brought to you for free and open access by the Science at ARROW@TU Dublin. It has been accepted for inclusion in Masters by an authorized administrator of ARROW@TU Dublin. For more information, please contact arrow.admin@tudublin.ie, aisling.coyne@tudublin.ie, vera.kilshaw@tudublin.ie.

School of Physics
Dublin Institute of Technology
Kevin Street, Dublin 8.

High-Speed

Electronic Speckle Pattern Interferometry

Carol Armstrong B.Sc.

December 2004

This thesis was prepared according to the regulations for postgraduate studies of the Dublin Institute of Technology and has been submitted for a Masters of Philosophy.

Supervised by

Dr. B. Bowe (DIT)

Dr. V. Toal (DIT)

Department of Physics

Declaration

I certify that this thesis which I now submit for examination for the award of the degree Masters of Philosophy, is entirely my own work and has not been taken from the work of others save and to the extent that such work has been cited and acknowledged within the text of my work.

This thesis was prepared according to the Regulations of Postgraduate studies by research of the Dublin Institute of Technology and has not been submitted in whole or in part for an award in other institute or university.

The Institute has permission to keep, to loan or to copy this thesis in whole or in part, on condition that any such use of the material of the thesis be duly acknowledged.

Signature C. Armstrong

Date 12/04

Acknowledgements

I would like to take this opportunity to thank my academic supervisor Dr. Brian Bowe for his help and assistance throughout the duration of my research. I would also like to express my gratitude to my advisory supervisor Dr. Vincent Toal. I must also acknowledge all at the Centre for Industrial & Engineering Optics in Kevin Street D.I.T. especially Sridhar Reddy-Guntaka for his time and assistance.

For their consistent encouragement I thank my family, especially my parents for their constant faith and motivation. I would also like to show my appreciation to my friends, Aurēlie, Blānaid, Carol, Joan and Maureen.

Abstract

Electronic Speckle Pattern Interferometry (ESPI) is used to measure surface displacements. Phase shifting can be used to obtain a fringe pattern which depicts the phase at every point in an image. Previous studies have used algorithms such as the 4-bucket algorithm to obtain phase maps of objects. After the object is displaced a second phase map is obtained in the same way and by correlation the phase difference due to the displacement can be determined. When the object is in rapid continuous motion these algorithms cannot be used.

Toward this end a 5-frame algorithm was written, in which the calibrated phase steps are obtained when the surface is at rest and an array of images are grabbed when the object is in motion at high speed. Any one of these images can then be used as the fifth image in the algorithm, thus allowing for calculation of phase change at any pixel at any instant of the motion of the surface.

The entire process is automated using LabVIEW software, which was specifically designed for the task. Both in-plane and out-of-plane systems were developed and calibrated. The systems were used to generate phase maps of an object undergoing motions at relatively high speeds.

Table of Contents

Declaration i

Acknowledgements ii

Abstract iii

Contents iv

1. Introduction 1

1.1 Non Destructive Testing 1

1.1.1 Ultrasonics 1

1.1.2 Acoustic Emission 3

1.1.3 Radiography 3

1.1.4 Magnetic Field Methods 4

1.2 Optical NDT Methods 6

1.2.1 Holographic Processes 6

1.2.2 Moirē Technique 8

1.2.3 Speckle Metrology 9

1.2.3.1 Electronic Speckle Pattern Interferometry 9

1.2.3.2 Shearography 12

1.3 Vibration Measurement Techniques 12

1.3.1 Accelerometers 12

1.3.2 Laser Doppler Vibrometers 12

1.3.3 ESPI for Vibration Measurement 13

1.4 Research Objective 16

2. Theory 17

2.1 Interferometry 17

2.2 The Speckle Effect 20

2.2.1 Speckle Size 22

2.3 Electronic Speckle pattern Interferometry 22

2.4 Correlation Fringes 23

2.4.1 Fringe Analysis 25

2.4.1.1 Phase Shifting Methods 27

2.5 In Plane Sensitive Interferometers 28

2.6 Out-of-plane sensitive Interferometers 29

2.7 Phase Shifting 30

2.7.1 Phase Shifting Algorithms 31

2.8 Phase Unwrapping 37

3. Experimental **38**

3.1 Set-up for ESPI Systems 38

3.1.1 In-Plane 38

3.2 In-Plane Calibrations 40

3.2.1 Conventional Camera 41

3.2.2 High Speed Camera 42

3.2.3 Phase-Shifting Calibrations 46

3.3 Phase Shifting Algorithms 47

3.3.1 4-Bucket Algorithm 47

3.3.2 5-Frame Algorithm 51

3.4 Phase-Shifting using a PZT 54

3.4.1 PZT Calibration 56

3.4.2 Comparison of 4-Bucket and 5-Frame Techniques 59

3.5 Application 60

4. Results **64**

4.1 In-Plane Calibrations 64

4.1.1 Conventional Camera 64

4.1.2 High Speed Camera 65

4.2 Phase Shifting Calibrations 70

4.3 PZT Calibration 71

4.3.1 Comparison of 4-Bucket and 5-Frame Techniques 74

4.4 Application 79

5. Conclusions **83**

6. References **86**

7. Appendices **89**

7.1 LabVIEW Software 89

7.2 Data 94

7.3 Equipment Specifications 109

CHAPTER 1 INTRODUCTION

1.1 Non Destructive Testing

Techniques used to examine an object, material or system without impairing its further usefulness are termed non destructive testing (NDT) methods[1]. NDT enables the gathering of data regarding the mechanical properties of a material, by evaluation of the deformation of the object under controlled loading conditions. With an understanding of the observed deformation, defects can be identified and located, and hence prevention of failure is possible, as samples with defects or inhomogenieties will cause non-uniform deformation. Some NDT techniques can even monitor the material for fatigue without a need for loading the object[1]. NDT methods have the advantage of being adaptable to automated production processes as well as to the inspection of localised problem areas. There are many techniques used to monitor motion caused by deformations, surface displacements, crack propagation and strain, including ultrasonics, acoustic emission, radiography and various optical methods. The following sections briefly outline these techniques.

1.1.1 Ultrasonic Testing

Ultrasound methods involve a transducer, which emits ultrasonic pulses within a frequency range of 20kHz and upward[1], coupled to one side of the test object. The pulses travel through the object and can be either diffracted, reflected or refracted by the defects or discontinuities within the material. A receiver placed on the other side of the material is used to detect the pulses. If a defect is encountered within the test object the amplitude of the signal will change accordingly.

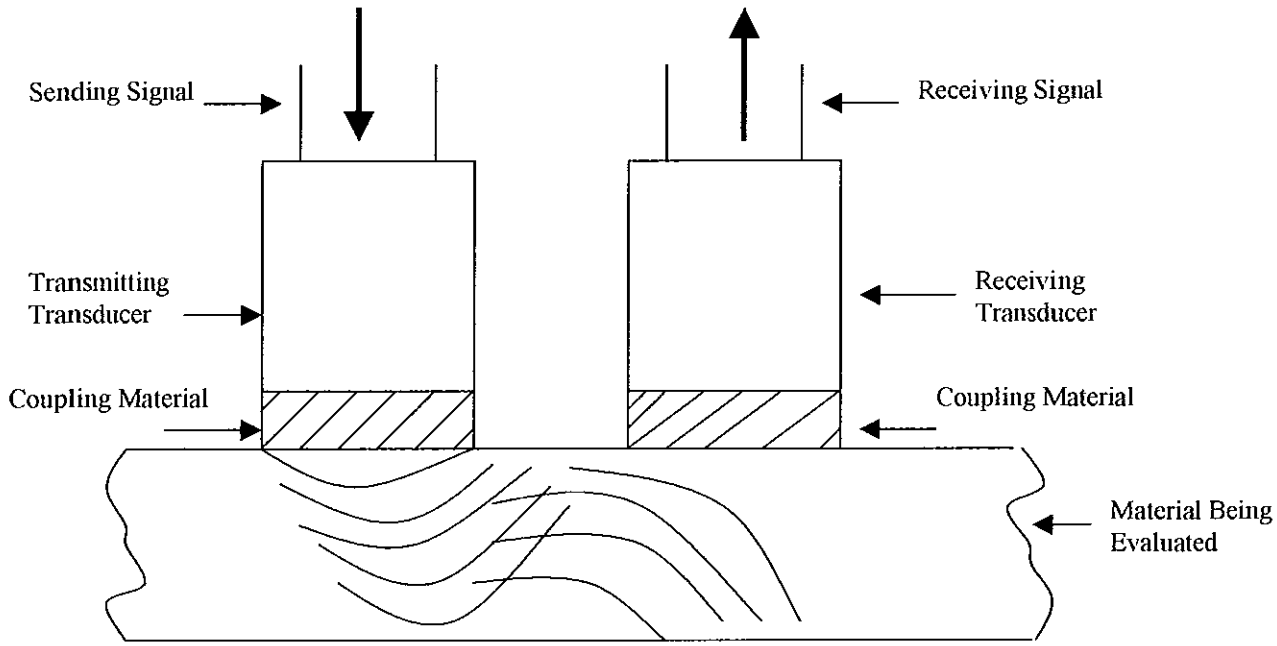

Figure 1.1 Set up for Ultrasonic Testing[3]

Ultrasonic inspection techniques include a range of probe arrangements, such as contact pulse echo, immersion pulse-echo, contact pitch-catch and immersion pitch-catch, see figure 1.1. Generally, these methods are most easily applied to simple, smooth surfaces with uniform geometry.

One major advantage this method has over other NDT procedures is that it allows for detection of defects deep within the material. However, the technique has the disadvantage of requiring complex image analysis and direct contact between transducer and object is required, thus decreasing the versatility of the method.

1.1.2 Acoustic Emission

Transient mechanical vibrations generated by rapid release of energy from localised sources within materials are termed acoustic emissions. Emissions are generated as a response to a stimulus and their energy levels can range from the displacement of a few dislocations to that needed to cause catastrophic cracking[4]. By detecting and monitoring these acoustic emissions, cracks and other defects can be discovered within a material. However, this technique is incapable of detecting a crack that is not undergoing growth, but with proper stimuli it can be used to monitor material behaviour of pressure vessels. This method allows the object to be monitored on a continuing basis and for examination of activity within the material.

1.1.3 Radiography

A radiographic image is basically a two-dimensional shadow picture of the intensity distribution of gamma rays after they have passed through the test object. The mass and type of defects present in the material cause the radiation to attenuate thereby yielding a corresponding intensity distribution. By using photographic film the radiation pattern can be made visible. Regardless of the medium used in the formation of the image the basic layout is as shown in figure 1.2. However, the system does pose a radiation hazard and therefore requires trained personnel. Another disadvantage is in the fact that cracks must align with beam axis in order to be detected at all.

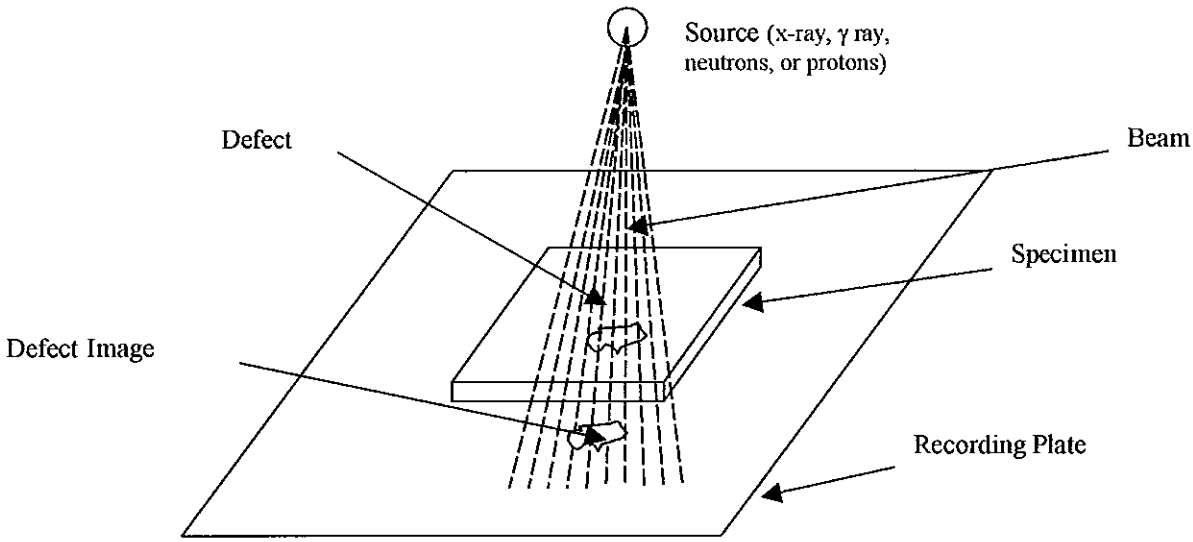

Figure 1.2 Layout for Radiographic Inspection[4]

1.1.4 Magnetic Field Methods

Procedures, which use magnetic fields as the essential component, are termed magnetic field methods. They include magnetic field perturbation (MFP) and electric current injection (ECI) [1].

In MFP testing a magnetic field is applied to a material which is permeable to magnetic fields. The permeability of the material along with the sensitivity of the probe determines the required field strength for this test procedure. Typically, the field strength will lie suitably below the saturation level. In general, the field is applied in a direction parallel to the test surface. Some applications to this method include determining the depth of case hardening and the carbon content[4].

An extension of the MFP method which is used in electrically conductive materials that are not magnetically permeable is called the ECI technique[4]. Electric current is injected into the test object between two points and a magnetic sensor monitors the magnetic field which results from the current. The defects in the material are determined by recording the magnetic field signals similar to the method used in MFP.

This method is relatively simple to carry out and will detect surface and near surface flaws, however, it cannot detect internal flaws and it also requires a high current to be applied which can cause damage to the system.

Some advantages and disadvantages to the above methods are outlined in table 1.1 below.

Method	Advantages	Disadvantages
Ultrasonic Testing	Allows for inspection deep within the material	Requires complex image analyses Contact with object
Acoustic Emission	Detects activities inside of materials Localization is made easy through time differential of signals Monitors continuously	Other methods are needed to provide quantitative results Signal discrimination and noise reduction are difficult
Radiography	No disassembly required Permanent Record Minimum preparation needed	Radiation hazard Trained personnel and film processing required Cracks must align with beam for detection
Magnetic Particle Inspection	Simple and easy to conduct Will detect surface and near surface flaws Sensitivity of testing can be specified and checked	Will not detect deep internal flaws High currents applied to component may cause damage Components usually have to be demagnetised

Table 1.1 Advantages and disadvantages to common NDT methods

1.2 Optical NDT Methods

Optical NDT uses light, often laser light, as the measurement tool. It can produce qualitative information, such as defect detection as well as quantitative data including surface displacement maps or stress/strain analysis. Optical NDT techniques can provide a full field analysis of an area without the detector coming in physical contact with the specimen. They have a high sensitivity and can, unlike other methods, provide information about the entire surface. Disadvantages include the fact that the systems must be calibrated regularly, they tend to be complex, expensive and are easily influenced by environmental conditions such as temperature and vibrations. However, these techniques can provide information regarding how the defects affect the behaviour of the object. Due to the submicrometer resolution, data can be obtained over a large object to a relatively high resolution. One of the most attractive advantages of optical testing for industry is that a very small non-destructive force is needed. This means that after testing is completed, if no defects are present, the object may return to the same condition as before. The following sections will briefly outline some optical NDT methods currently in use.

1.2.1 Holographic Processes

The principle of holographic interferometry is that it records the complete pattern of waves, in both amplitude and phase, reflected by an object. A basic holographic set up is shown in figure 1.3. The laser beam is spatially filtered and expanded; part of it is then incident upon the object and it is reflected onto a photosensitive emulsion. A mirror alongside the object reflects another part of the beam onto the emulsion. This is known as the reference beam. Thus we have light from the object and reference mirror interfering at the emulsion. After processing it is possible to reconstruct an image of the object superimposed on the object itself. Then when the object is loaded interference will occur between the loaded object light and reconstructed image light. The interference pattern is indicative of the change that has occurred.

Surfaces as well as sub-surface defects show distortions in the otherwise uniform pattern. In addition, the characteristics of the component, such as vibration modes, mechanical properties, residual stress etc. can be identified through holographic inspection.

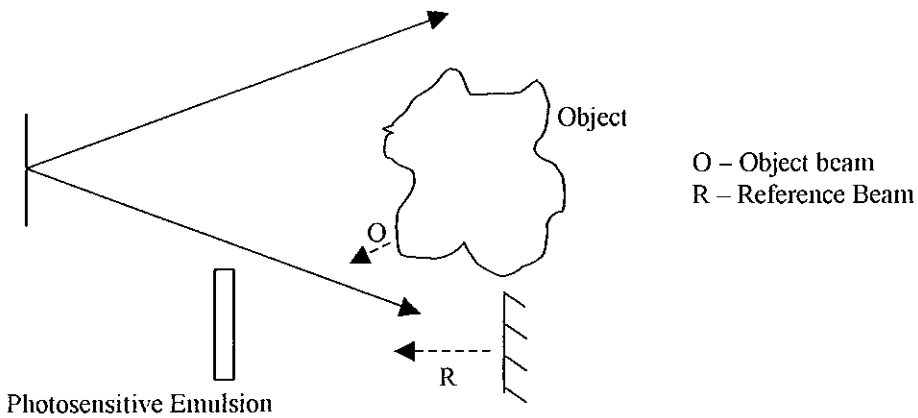

Figure 1.3 Basic Holographic Interferometer

Holography has the advantages of being very sensitive and highly versatile, however, it does suffer from adverse environmental conditions such as vibrations and temperature.

The requirement to develop plates has curtailed the use of this technique and it has the added disadvantage in that it is difficult to independently measure displacements in different planes.

1.2.2 Moiré Methods

When two gratings are laid in contact with a slight angle between the lines a fringe pattern is observed, with a lower frequency than that of the gratings. The resulting fringe pattern is called a Moiré pattern and can be created by various types of gratings including circular, radial, spirals etc.

If a grating is attached to an object and another grating projected onto it any movement of the surface will cause a relative movement between the gratings producing a pattern of Moiré fringes, whose spatial frequency and alignment represent the movement that occurred. The sensitivity of this method will depend on the image analysis technique and the spatial frequencies of the original gratings. However, these gratings can have very high spatial frequencies allowing for a high sensitivity.

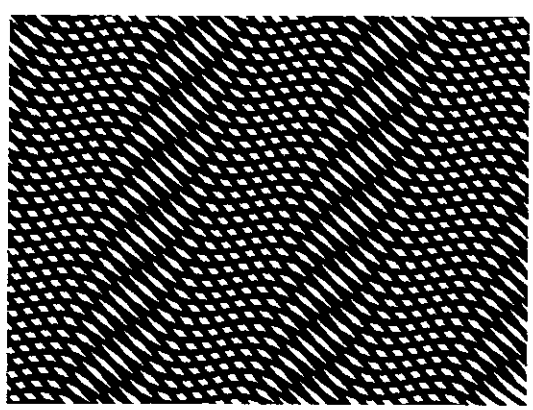

Figure 1.4 Typical Moirē Pattern

1.2.3 Speckle Metrology

The coherent nature of laser light leads to the appearance of the phenomenon known as speckle, that is, the grainy appearance of a scattering surface when illuminated by coherent light. The speckle arises due to the interference that occurs between the light rays as they are scattered by different points on the surface[5]. Speckle techniques are very useful and powerful tools in measuring surface displacement as they are simple and versatile. They can be adapted to suit different applications, such as deformation measurements, strain analysis, crack propagation (see figures 1.5 and 1.6) and to monitor surface vibration They can be set up to measure in-plane and out-of-plane movement separately or simultaneously to get complete 3D displacement measurements. Like many other optical techniques, they are whole field, non-destructive and can be real time. There are various NDT techniques which utilise the speckle effect including speckle photography, speckle-shearing interferometry and electronic speckle pattern interferometry.

1.2.3.1 Electronic Speckle Pattern Interferometry (ESPI)

The principle of ESPI is outlined in section 2.3 of this thesis. In speckle photography the speckles themselves undergo the displacement, however in ESPI the movement of the object causes a change in path difference, and hence a phase difference, between two beams illuminating the surface which causes a change in resultant intensity across the area. ESPI cannot measure a large field of strain distributions and suffers from decorrelation, but it nevertheless has many advantages. It is a non-contact method, it is portable and can be run from a PC. These advantages make it possible to use ESPI for strain analysis, deformation measurements and in studies of crack propagations. In figure 1.5 a crack tip is seen as the point towards which the fringes converge. In the first pattern on the left the crack has only begun to grow and it travels up along the specimen as shown in the second pattern. The third pattern was taken just before the specimen broke, illustrating the use of ESPI as an optical NDT technique.

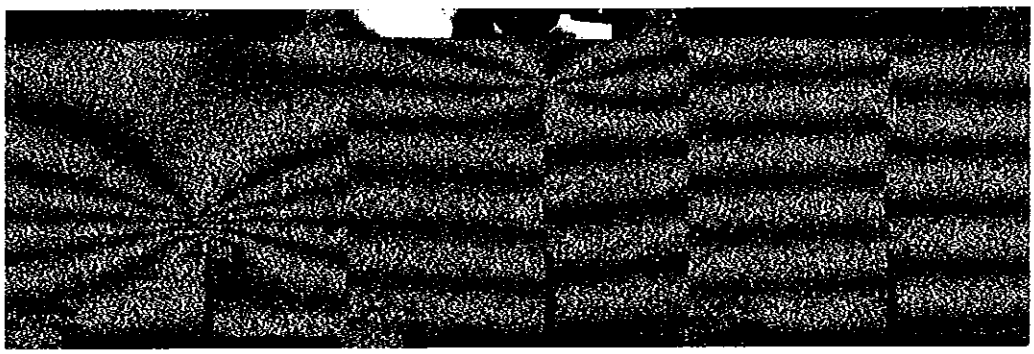

Figure 1.5 Propagation of a crack in a notched clay sample[27]

A comparison of several optical NDT methods is shown in table 1.2.

Method	Advantages	Disadvantages
Holography	Versatile High sensitivity Direction of sensitivity clearly defined	Sensitive to environment Difficult to separate superposition of effects Inability to independently measure displacements in different planes
Moire	Relatively sharp fringe patterns	Grating must be in contact with the surface for strain measurement
Speckle Photography	Less sensitive to disturbances No surface preparation Non contacting strain gauges possible Additional information from speckle decorrelation	Limited spatial resolution Needs careful calibration of optical set-up (strain fields)
ESPI	Real-time correlation Portable Can be automated with PC	ESPI cannot measure a large field with a wide dynamic range of strain distributions

Table 1.2 Advantages and disadvantages of optical NDT techniques[2-4]

1.2.3.2 Shearography

Shearography is another speckle interferometric method, but it allows full-field observation of surface displacement derivatives[25]. By looking for flaw-induced strain anomalies it reveals flaws in materials. In this technique two images are produced and laterally sheared with respect to each other. The deformation gradient of the surface is represented by the speckle interference pattern. However, due to the fact that it is the gradient which is represented, the systems are insensitive to rigid body movements and thermal fluctuations[4]. The main application, therefore, of this method is defect recognition.

1.3 Vibration Measurement Techniques

1.3.1 Accelerometers

Three major quantities are of interest in vibration studies; the vibration displacement, velocity and acceleration. An accelerometer is an electromechanical transducer which produces, at its output terminals, a voltage or charge that is proportional to the acceleration to which it is subjected. Accelerometers consist of piezoelectric crystals and a mass normally enclosed in a protective metal case[21]. The crystal creates a charge, which is proportional to the acceleration. The sensor will have either an internal or external charge amplifier, which converts the charge output of the crystal to a voltage. Accelerometers can be selected depending on the frequency range required.

1.3.2 Laser Doppler Vibrometry (LDV)

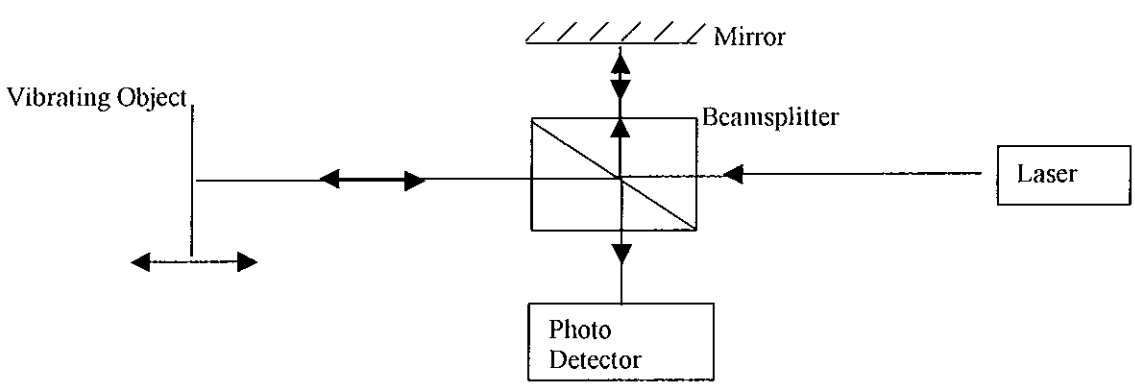

Figure 1.6 Laser Doppler Vibrometer

The principle behind LDV is based on the detection of a Doppler frequency shift in coherent light scattered by the target. In the case of LDV the beam hits the vibrating object as it is in motion. Figure 1.6 shows the beam incident upon a beamsplitter and directed onto the target object. As the object moves Δf changes (i.e. the difference between the frequencies of the transmitted and the returning beams) and by using a frequency to voltage converter a voltage which represents the motion undergone by the object can be obtained.

1.3.3 Electronic speckle pattern interferometry for vibration measurement

There have been several methods designed to use speckle interferometry as a method to measure vibrations. They include using speckle contrast, utilising pulsed lasers and the use of high-speed cameras.

A theory[15] has been outlined which gives the contrast of the speckles as a function of the beam ratio used and the amplitude of vibration. In the same areas in which bright fringes are traditionally found, areas of higher contrast are detected. Nodal lines appear in such areas, while anti-nodal lines show blurred speckles.

High speed ESPI with a pulsed laser has been utilised in the study of brake disc modal behaviour[17]. This method is not commonly used due to the fact that pulsed lasers are relatively expensive, not very portable and are difficult to use.

High-speed ESPI has also been used to measure non-harmonic vibrations. A fibre optic delivery system can be used in conjunction with a low-power laser and a the high framing rate CCD camera. Vibrations with both high temporal and spatial resolutions can be measured with this technique, an advantage not offered by alternatives such as a scanning laser vibrometer.

The use of high-speed ESPI together with a wave-guide phase modulator has lead to the observation of out-of-plane vibrations of up to 100kHz[19].

The research reported in this thesis uses a high-speed camera to grab the images at up to 4000/s, thus allowing for observation of high-speed vibrations. This research uses a high-speed camera in conjunction with new algorithms, and utilises the captured images to produce a phase map of the high-speed displacement. The theory behind this method leads to the calculation of the high-speed displacement of any pixel at any instant in its recorded motion.

Table 1.3 shows some of the advantages and disadvantages of the above techniques

Method	Advantages	Disadvantages
Transducers	Can be placed in awkward parts of a machine Broad frequency range	Must come in contact with object Can only detect vibration on specific area
Accelerometers	Can be selected for required frequency	Limited dynamic range
Laser Doppler Vibrometers	No need for prior knowledge of the object's parameters Capable of high bandwidths	Complex Expensive
ESPI	Non contact Full field	Interpretation of the result not immediate Setting up time quite long

Table 1.3 Advantages and disadvantages of vibrational measurement techniques

1.4 Research Objective

When high-speed ESPI is used to measure rapid motions, such as vibrations, traditional algorithms become obsolete, as it is not possible to grab images of the movement using conventional cameras without loosing a lot of data. As a result high-speed ESPI uses post process data analysis techniques. In order to produce a phase map using high-speed ESPI new algorithms have had to be written.

The purpose of this research was the design, construction and testing of an ESPI system for applications in vibration monitoring. The project aimed to produce a system that is robust, compact and computer controlled. The technique developed, uses a high-speed CCD camera in order to grab frames at a rate of up to 4000 frames per second, thus minimizing the amount of data lost. The use of LabVIEW software allowed for the set up to be integrated with a PC for both data acquisition and analysis. New algorithms were developed to allow for post processing of the gathered data. It was also essential that the system be made portable. This aspect is important as a major disadvantage to these systems has been the need to bring the test object to the laboratory and this has made industry reluctant to adopt these techniques.

The plan for the project was to initially carry out a literature review in the areas of ESPI and vibrations. Following this the system would be designed to comply with the requirements discussed above. After extensive testing the system would be used to obtain results for a specific application.

The next chapter deals with the fundamental aspects of ESPI. Both the various phase shifting algorithms as well as fringe analysis methods are examined.

CHAPTER 2 THEORY

2.1 Interferometry

Coherent sources have a very narrow frequency bandwidth and so produce waves with a constant phase. If a coherent beam is split in two and these beams are overlapped, then in order for complete cancellation of the beams to occur the amplitudes of the superposing waves must be equal. If their phase difference is not constant, at a certain point there may be reinforcement at one instant and cancellation at the next. If these variations follow one another rapidly the effect is to produce uniformity of field.

Interference occurs when two or more waves overlap in space. If I_1 and I_2 are the intensities of the two component waves and ϕ_1 and ϕ_2 are the corresponding phases then $\Delta\phi$ is the phase difference, $(\phi_1-\phi_2)$, the resultant intensity I is[10]:

$$I = I_1 + I_2 + 2\sqrt{I_1 I_2}\cos\Delta\phi$$

Assuming that the components have equal amplitudes, $I_1 = I_2 = I_0$ and

$$I = 2I_0 + 2I_0\cos\Delta\phi$$

$$\Rightarrow \qquad I = 2I_0[1+\cos\Delta\phi] \qquad \text{Equation 2.1}$$

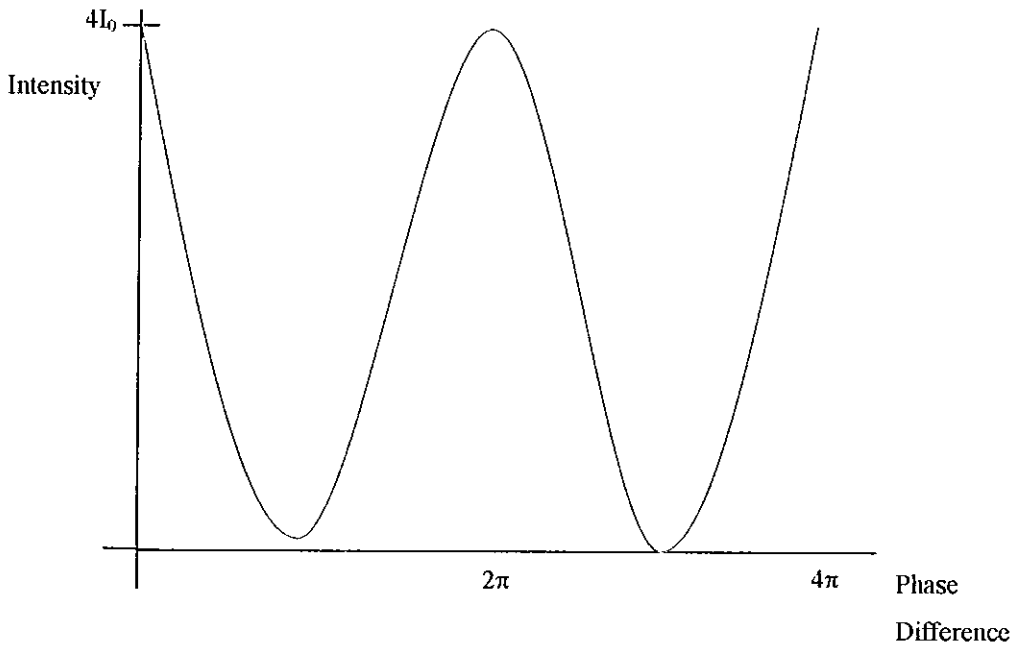

Figure 2.1 Graph of the intensity of the interference as a function of phase

Therefore, if $\Delta\phi = 2n\pi$, where n=0,1,2,3..., maximum intensity occurs of $4I_0$. When $\Delta\phi=(2n+1)\ \pi$, minimum intensity occurs at 0. Figure 2.1 shows a graph of the resultant intensity as $\Delta\phi$ is varied. It can be seen that as the phase is changed the intensity changes in a sinusoidal way.

Interferometers are very important measuring tools as they provide an accuracy to the order of one wavelength of the light used[6] for fringe measurements. The principal of interferometry is that a path difference between two coherent light beams will produce an interference pattern of light and dark fringes.

The resulting fringes will be very close together unless the angle θ between the two beams is small. Many procedures for combining two wavefronts at such small angles have been used. The Michelson interferometer is one such important instrument, it achieved the first accurate measurement of the speed of light and its configuration is shown in figure 2.2.

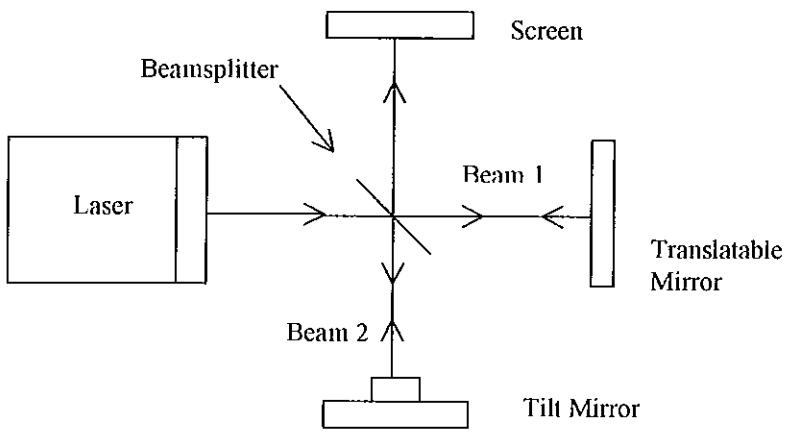

Figure 2.2 A typical Michelson Interferometer[10]

In figure 2.2 it can be seen that the light from the laser first strikes the beamsplitter dividing it into two equal amplitude beams: a transmitted one, Beam 1, and a reflected one, Beam 2. It is here assumed that the back surface of the beam splitter is the coated surface. Beam 1 travels to the translatable mirror of the interferometer, which can translate back and forth in order to provide a desired path length difference, between the paths travelled by Beams 1 and 2. Beam 1 reflects off of the translation mirror and travels back to the beam splitter, where it is split into two equal amplitude beams. The beam to be measured is the one that reflects off the beam splitter and travels to the screen[7].

Beam 2 travels from the beam splitter to the "tilt" mirror. In the interferometer this mirror can only be rotated about its vertical axis. The beam then reflects from the tilt mirror and travels back to the beam splitter. At the beam splitter, Beam 2 is divided into equal amplitude reflected and transmitted beams, with the transmitted beam travelling to the screen where it interferes with the Beam 1 forming a fringe pattern.

There are many types of interferometers, however, the type used in this research is an electronic speckle pattern interferometer. The theory of speckle and how it can be utilised to create an interferometry system is now discussed.

2.2 The Speckle Effect

The coherence of laser light leads to the appearance of the phenomenon of speckle, that is, the grainy appearance of a scattering surface when illuminated by coherent light. In order for the speckle effect to occur the surface must be optically rough. This means that the roughness of the surface must be in the order of, or greater than the wavelength of the light illuminating it. The speckle effect arises due to the interference that occurs between the light rays as they are scattered by different points on the surface.

In order to find a representative value for the speckle size, consider figure 2.3:

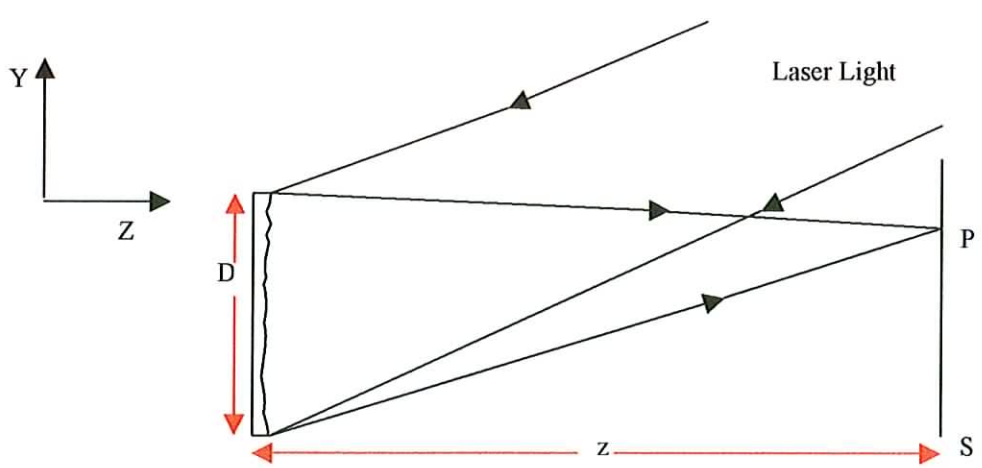

Figure 2.3 Formation of Objective Speckle

Here, over an area of cross section D, a laser illuminates an optically rough surface. The speckle pattern is formed a distance z from the object at a screen S. Only the intensity variations along the y-direction will be considered.

When two points on a speckle pattern are close their intensities will be closely related. As the distance between them increases they become gradually unrelated. The correlation function, R, gives the relationship of the intensities as a function of the distance between them. Taking <I> as the mean intensity and the distance as zero

$$R = \langle I^2 \rangle$$

The distance at which the intensities become unrelated provides an estimate for the size of the speckles. For a surface of dimensions DxD illuminated by a uniform beam, the average size of a speckle is found to be

$$\delta_0 = \frac{\lambda z}{D}$$

where z is the distance between the viewing and object planes.

Figure 2.4 illustrates a coherent beam from a laser diode illuminating the rough surface of an object resulting in a speckle pattern.

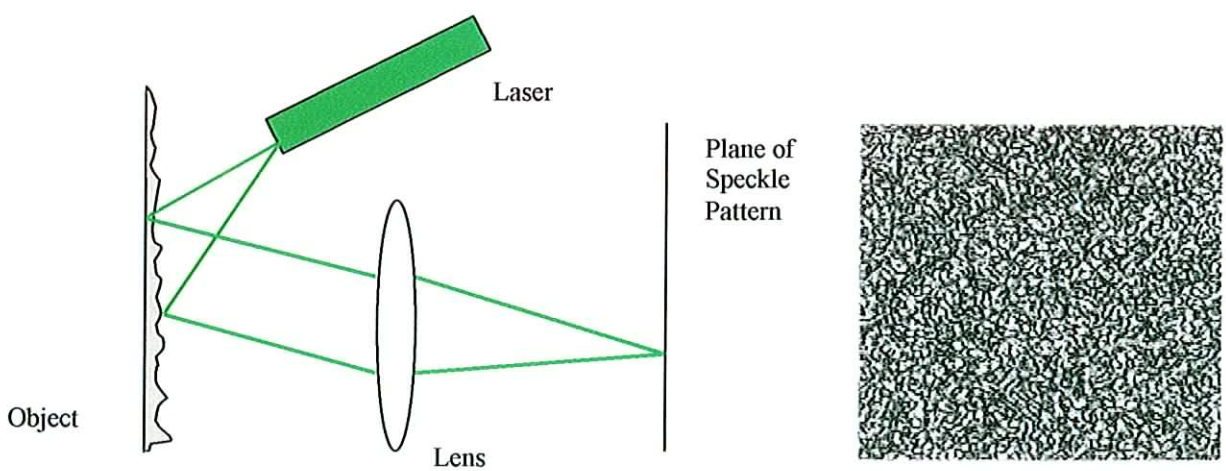

Figure 2.4 Formation of speckle pattern

1.2.1 Speckle size

The speckle size is an extremely important characteristic of the pattern. This is due to the fact that when imaging a speckle pattern onto a CCD array, optimum fringe quality is achieved when the speckle size is equal to that of one pixel on the CCD array.

When no lens is used the observed pattern is termed an objective speckle pattern and the size of the speckles depends on the aperture used and the wavelength of the laser. However, since a lens is used in this case, this pattern is termed subjective speckle and so the aperture of the lens is the important variable, the size of the speckles being inversely proportional to the size of the aperture.

2.3 Electronic Speckle Pattern Interferometry

As stated previously, when two coherent light sources overlap an interference pattern is observed. Within an in-plane ESPI system the beam from the laser is split into two parts, I_1 and I_2, of equal intensity. Each one is guided to the object where they form two independent speckle patterns, these patterns interfere to form a resultant speckle pattern. ESPI uses a CCD camera to acquire the images and computer software with a frame grabber to record an image of this first resultant speckle pattern. When the object is displaced a phase change is introduced between the two beams and this leads to a change in the intensity of the interference pattern. This second resultant speckle pattern is subsequently grabbed by the CCD camera and saved. The PC then correlates these speckle patterns to form a fringe pattern, whose appearance, i.e. spatial frequency and orientation, represents the surface displacement.

Figure 2.5 illustrates the speckle pattern both before and after the induced phase shift and the fringe pattern, which results from correlation.

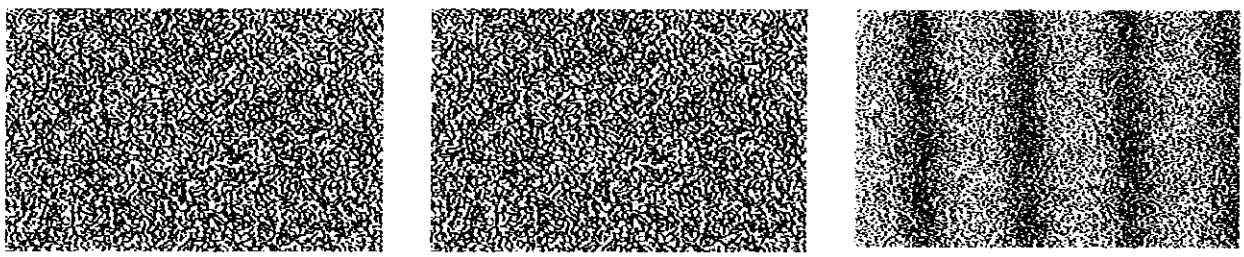

(a) (b) (c)

Figure 2.5

(a) – Resultant Speckle Pattern

(b) – Resultant Speckle pattern after phase change

(c) – Fringe Pattern resulting from correlation

2.4 Correlation Fringes

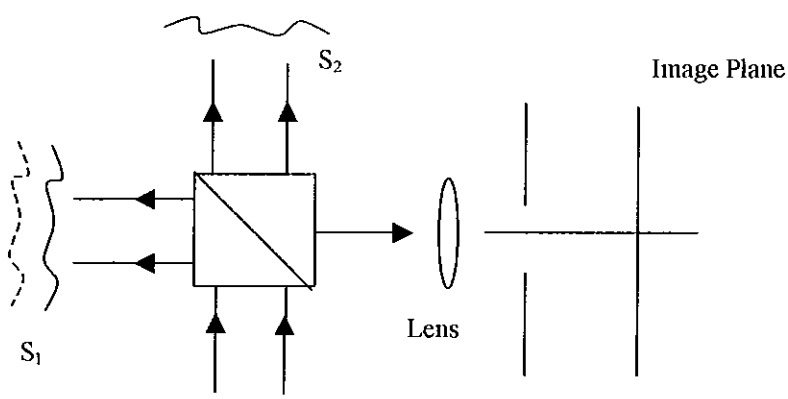

Figure 2.6 Michelson out-of-plane system

On recombination at the beamsplitter the two wavefronts scattered from S_1 and S_2 interfere and the result is recorded at the image plane of the lens, see Figure 2.6. The intensity distribution in this image plane is given by

$$I = I_1 + I_2 + 2\sqrt{I_1 I_2}\cos\varphi \qquad \text{Equation 2.2}$$

where φ is random, i.e. it depends on the surface height variations, and therefore the resultant intensity varies for each point across the surface.

When S_1 is displaced a distance d normal to the surface, i.e. out-of-plane, a phase change $\Delta\phi$ arises

$$\Delta\phi = \frac{4\pi d}{\lambda}$$

this changes the intensity at the point to

$$I' = I_1 + I_2 + 2\sqrt{I_1 I_2}\cos(\varphi + \Delta\phi) \qquad \text{Equation 2.3}$$

In order to gain an expression for the fringes equations 2.2 and 2.3 are substituted into the correlation coefficient[5] $\rho(\Delta\phi)$ yielding:

$$\rho(\Delta\phi) = \frac{1}{2}(\cos\Delta\phi) \qquad \text{Equation 2.4}$$

By correlation of I and I' it can be shown that when

Unity $\Rightarrow \Delta\phi = 2n\pi$ $\Rightarrow$ $\rho(\Delta\phi) = 1$ $\Rightarrow$ max correlation $\Rightarrow$ bright fringe

Zero $\Rightarrow \Delta\phi = (2n + 1)\pi$ $\Rightarrow$ $\rho(\Delta\phi) = 0$ $\Rightarrow$ min correlation $\Rightarrow$ dark fringe

The variation in correlation represents the change in the displacement of the object surface. When there is no displacement, maximum correlation occurs and a bright fringe is observed; a dark fringe is seen when minimum correlation occurs.

This correlation process can be carried out using subtraction and rectification. Subtracting the initial speckle pattern (Equation 2.3) from the second speckle pattern (Equation 2.2) and rectifying the result produces an image whose intensity I, at any point (x,y) is given by

$$I = 4\left[I_O I_R \sin^2\left(\phi + \frac{1}{2}\Delta\phi\right)\sin^2\frac{1}{2}\Delta\phi\right]^{1/2} \qquad \text{Equation 2.5}$$

It is important to note that substituting $2n\pi$ now yields a dark fringe and $(2n + 1)\pi$ results in a bright fringe. However, for analysis purposes equations 2.4 and 2.5 represent the same thing, as it is only the relative surface displacement that is of interest.

2.4.1 Fringe Analysis

When ESPI is performed on an object the result is the construction of a fringe pattern which represents the displacement. The resulting fringe pattern can be used to observe cracks or anomalies in structures, to measure deformations and analyse stress. This can be either a qualitative or a quantitative procedure. Qualitative analysis can be carried out on these patterns using visual inspection and this can sometimes be sufficient as in the case of crack detection. However, with the decreasing cost of digital imaging equipment, digital fringe analysis techniques have been developed to relatively high levels, allowing for accurate quantitative analysis.

Figure 2.7 shows a theoretical pattern of displacement fringes. The fringes are first counted as shown.

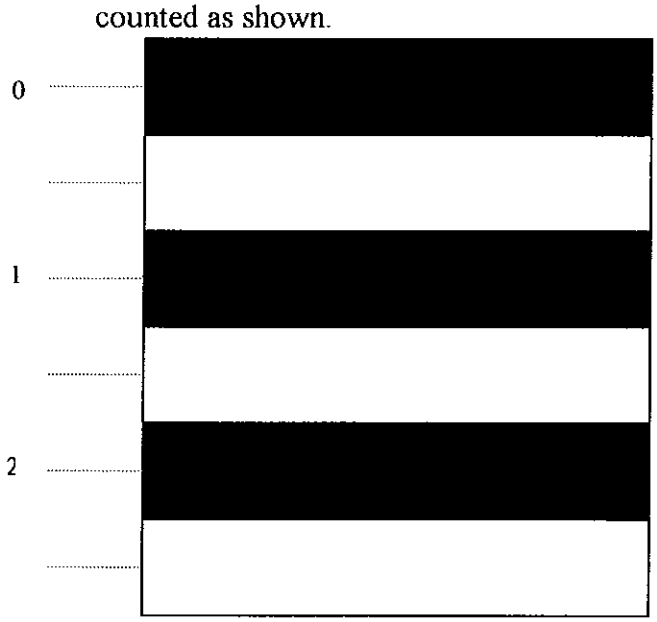

Note: These are square waves but are only used here to illustrate the method for counting the number of fringes obtained

Figure 2.7 A pattern of displacement fringes and its waveform

The number of fringes, N, is used to calculate the relative displacement between any two points on the surface which caused the fringe pattern to form. In the case of an in-plane displacement:

$$d = \frac{N\lambda}{2\sin\theta}$$

d is the displacement / m

λ is the wavelength / m

θ represents the angle between the beams

For example, if there were two fringes formed between two points on the surface and the angle between the two beams, λ of 785nm, was measured at 30^0 then d is calculated as

$$d = \frac{2(785\times10^{-9})}{2(\sin 30)} = \frac{1.57\times10^{-6}}{2(0.5)} = 1.57\mu m$$

There are some inherent disadvantages to this method however. Unless the zero order is known and the motion of the fringes can be observed, the direction of, and the exact value of, the displacement cannot be calculated. Also, the process is based on accurate counting of the fringes. In reality the fringes are relatively noisy, due to the nature of speckle, making it quite difficult to locate the centre of the fringes accurately. At best a resolution of up to λ/10 is achievable using the fringe counting method.

To counteract this disadvantage phase fringes can be used in place of the displacement fringes. There are a number of ways to do this including phase shifting and various Fourier methods which have the advantage of only requiring a single pattern[14].

2.4.1.1 Phase Shifting Methods

Phase shifting methods involve generation of a modulo 2π phase map such as the one shown in figure 2.8.

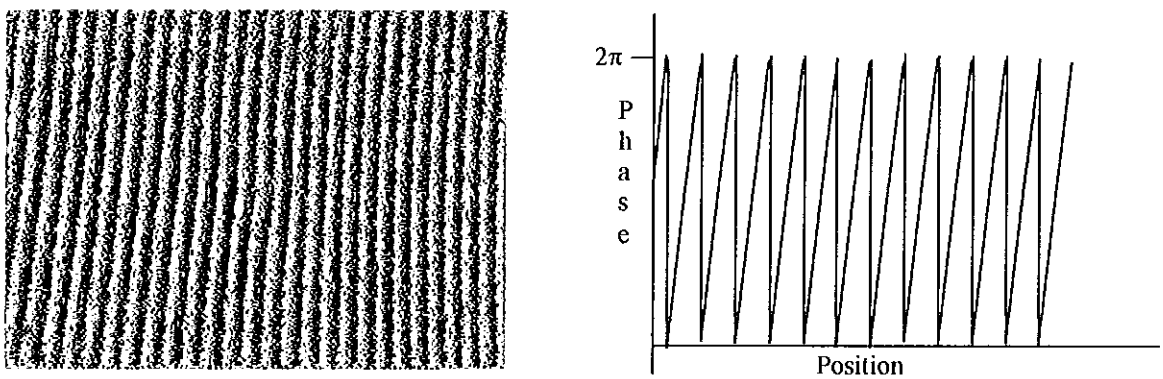

(a) Modulo 2π phase map (b) Ramped profile of fringes from section of phase map

Figure 2.8 Wrapped Phase Map

By inspection, it can be seen that accurate location of the peaks is significantly easier than with the displacement fringes. With displacement fringes the error can be in the order of half a fringe whereas with phase maps the error is significantly reduced. Under optimum conditions resolutions of $\lambda/100$ are now possible.

However, this method does pose its own problems in that the formation of a phase map requires introducing accurately controlled phase shifts between the interferometer beams. Furthermore, to gain an absolute displacement map the wrapped map must be unwrapped, as illustrated in figure 2.9. This requires the detection and removal of the 2π jumps.

There are various methods which can be used to introduce the required phase shift into the system. They include modulation of the laser or introducing a controlled movement into one of the beams by, for example, attaching a PZT to one of the mirrors in the interferometer.

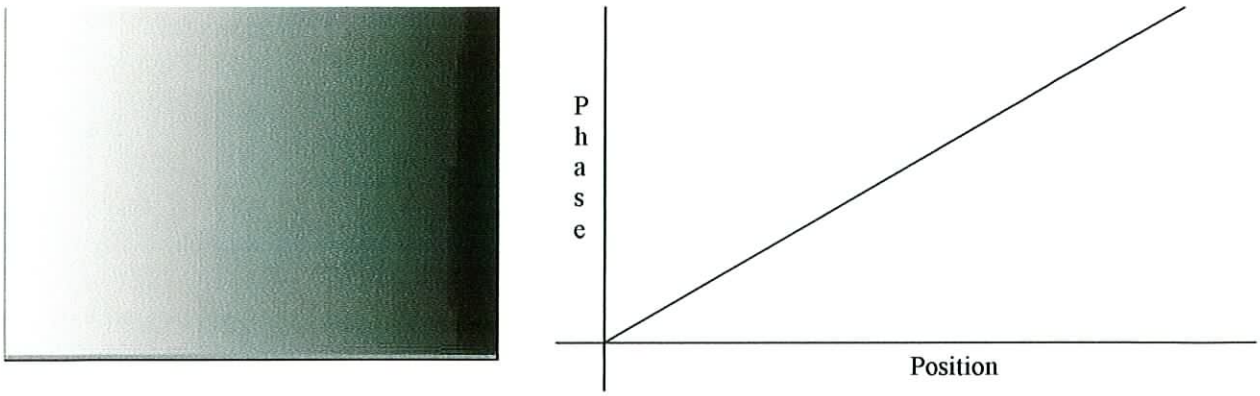

Figure 2.9 Unwrapped Phase Map

2.5 In-plane displacement sensitive interferometers

The set-up in figure 2.10 gives rise to fringes which are sensitive to in-plane displacements, i.e. along the x_2 direction. Two plane wavefronts, I_1 and I_2 are inclined at opposite and equal angles, θ, to the x_1-axis surface normal. These wavefronts illuminate the object, which lies in the x_2, x_3 plane.

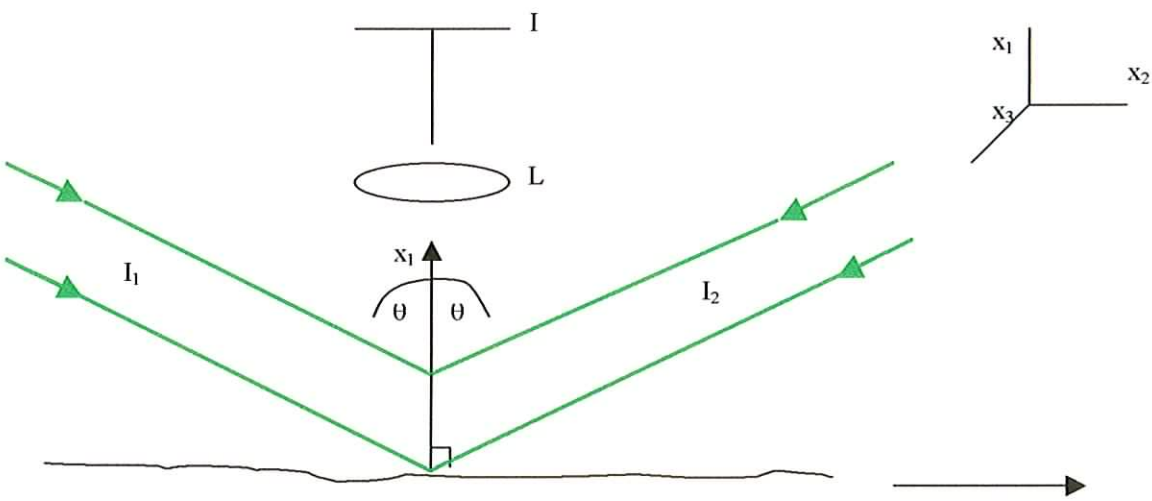

Figure 2.10 In-plane displacement set up

A displacement, d_2, of the surface along the x_2 direction causes a relative phase change between these two beams. This phase change, $\Delta\phi$, can be expressed by the equation[6]

$$\Delta\phi = \frac{4\pi}{\lambda} d_2 \sin\theta$$

Since the relative phase of the wavefronts is constant over planes parallel to the x_1x_3-plane, the displacement components d_1 and d_3 which lie in those planes, will introduce no phase change. Therefore, in the presence of out-of-plane displacements, this type of interferometer allows in-plane displacement distributions to be observed independently.

2.6 Out-of-Plane Sensitive Interferometers

The out-of-plane set-up, as shown in figure 2.11, can be briefly described as follows. A laser beam is split into two, with one of the beams, the object beam, used to illuminate the object. A CCD camera is then used to view the illuminated object. The other beam, which is called the reference beam, is directed in such a way that it intersects the line of view between the object and video camera. At that point, a semi-silvered mirror is used to deflect the reference beam into the camera causing it to combine with the light reflected from the object. Due to the monochromatic properties of the laser light, the object and reference beam interfere to produce a unique resultant speckle pattern. Any out of plane displacement of the object will introduce a phase shift between the object and reference beam with in turn results in a change in intensity in the resultant speckle pattern. By correlating the two resultant speckle patterns a fringe pattern which represents the out of plane movement can be obtained. It is also possible to combine both the in plane and the out of plane methods to produce a dual ESPI system, i.e. one which is capable of measuring motions in both directions.

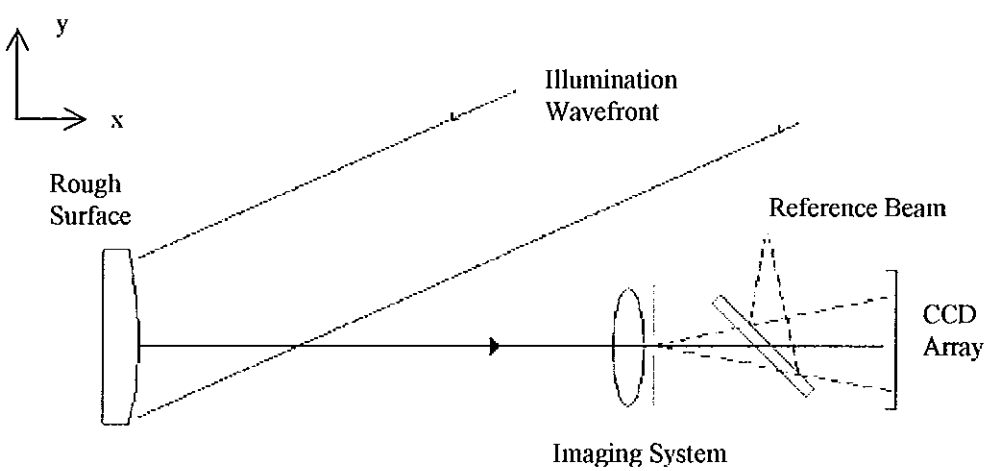

Figure 2.11 Out-of-plane displacement set up

2.7 Phase-Shifting

Phase shifting interferometry can be used to obtain the phase distribution, the phase map, of an object wave from a sequence of interference patterns. The object wave can also contain information about any phase object, such as the quality of an optical element, or a fluid property distribution.

An interferogram can be represented by the following equation[8]:

$$I(x,y) = \bar{I}(x,y)\{1 + \eta(x,y)\cos[\theta(x,y) + \Delta\phi(x,y)]\}$$

Here (x,y) refers to each pixel in the pattern, I is the recorded intensity, $\bar{I}$ is the average intensity of the object plus the reference beam, η is the fringe contrast, θ is the phase of the object wave, and $\Delta\phi$ is the relative phase between the object and reference waves. If $\Delta\phi$ can be controlled, and if $\bar{I}$ and η can be stabilised so they don't change, then several frames of the pattern can be recorded and used to calculate the object wave phase distribution θ. The frames will differ from each other only by the value of $\Delta\phi$[11].

When two mutually coherent light beams are superimposed an interference pattern is observed. The resulting intensity, I, at any point (x,y) in this pattern can be described by

$$I = I_1 + I_2 + 2\sqrt{I_1 I_2}\cos(\Delta\phi)$$

When the object is then displaced, by an amount which is suitably small leaving $I_1 + I_2$ unchanged and only changing ϕ by δ, equation 3.5 becomes

$$I' = I_1 + I_2 + 2\sqrt{I_1 I_2}\cos(\Delta\phi + \delta)$$

2.7.1 Phase Shifting Algorithms

In its infancy ESPI was not widely used in industry because it had very little practical application. However, with the developments in phase shifting and unwrapping algorithms, CCD technology and image processing, the ESPI technique has become a common optical method for deformation testing.

Several techniques have been developed which shift the phase of one beam with respect to the other and measure the intensity of the resulting pattern at relative phase steps. In this section a number of these techniques are outlined.

Credit for the first publication on phase shifting interferometry (PSI) is usually given to Carrē (1966)[14]. However, the algorithm itself is no longer widely used due to the introduction of large errors arising from phase shifting nonlinearities.

Here, knowledge of the phase shift between consecutive frames is not required as long as phase steps are constant. Usually a phase shift of α between frames resulting in the following

$$I_1 = 0$$
$$I_2 = 2I_0[1+\cos(\Delta\phi+\alpha)]$$
$$I_3 = 2I_0[1+\cos(\Delta\phi+2\alpha)]$$
$$I_4 = 2I_0[1+\cos(\Delta\phi+3\alpha)]$$

This yields

$$\alpha = 2\tan^{-1}\left[\sqrt{\frac{3(I_2-I_3)-(I_1-I_4)}{(I_2-I_3)+(I_1-I_4)}}\right] \qquad \text{Equation 2.9}$$

Equation 2.9 is known as the Carrē algorithm. This algorithm is useful as the specific value used for the phase step is unimportant, provided that the shift is constant between frames. However, as previously stated, it has limitations with respect to error that are important.

Another such algorithm is known as the *four-bucket algorithm*, which can be used to map the phase of an object at rest. This is achieved by recording a series of frames with the object at rest but with various phase shifts. Let ϕ represent the initial random speckle phase. The four phase steps are: 0, $\pi/2$, π and $3\pi/2$ respectively. The resulting equations are as follows:

$$I_0 = I_1 + I_2 + 2\sqrt{I_1 I_2}\cos(\Delta\phi)$$

$$I_{\pi/2} = I_1 + I_2 + 2\sqrt{I_1 I_2}\cos(\Delta\phi + \pi/2)$$

$$I_\pi = I_1 + I_2 + 2\sqrt{I_1 I_2}\cos(\Delta\phi + \pi)$$

$$I_{3\pi/2} = I_1 + I_2 + 2\sqrt{I_1 I_2}\cos(\Delta\phi + 3\pi/2)$$

The phase at each point can thus be given by the expression[3]:

$$\Delta\phi = \tan^{-1}\frac{I_{3\pi/2} - I_{\pi/2}}{I_0 - I_\pi} \qquad \text{Equation 2.8}$$

Equation 2.8 is known as the 4-bucket algorithm. This results in a phase map of the surface under observation. There is a variance on this called the 5-bucket algorithm which achieves the same aim as the 4-bucket algorithm, but requires one extra phase shift. The more images taken the more accurate the result, however this depends on the phase steps being accurately controlled. For this reason the algorithm devised for this research was termed the 5-frame technique to avoid confusion.

An alternative algorithm, devised in 1998, was introduced by Angel and Wizinowich and was termed the (2+1) algorithm. This technique deals with errors which result from unwanted vibrations. Here, two patterns are quickly recorded and a third is taken which is the average of the initial two. The steps are, therefore, 0, $-\pi/2$, and 0, π. The frames are as follows:

$$I_1 = I_0[1+\varphi\cos\Delta\phi]$$

$$I_2 = I_0\left[1+\varphi\cos\left(\Delta\phi-\frac{\pi}{2}\right)\right] = I_0[1+\varphi\sin\Delta\phi]$$

$$I_3 = \frac{1}{2}\{I_0[1+\varphi\cos\Delta\phi]\}+\frac{1}{2}\{I_0[1+\varphi\cos(\Delta\phi+\pi)]\} = I_0$$

This gives

$$\Delta\phi = \tan^{-1}\left(\frac{I_2-I_3}{I_1-I_3}\right) \qquad \text{Equation 2.10}$$

In order to obtain the first two images this approach utilises the interline transfer CCD. In such a CCD there is a storage pixel adjacent to each photosite. While the photosites are integrating the light, the storage pixels produce the video signal. The storage sites are now empty and free to collect the next, rapidly acquired, video signal[14].

There are limitations, however, to this method. It is susceptible to errors due to the decreased number of data frames taken.

The minimum number of images required to reconstruct the wavefront is three[8]. The *three-frame technique* is based on this premise, which, using α values of $\pi/4$, $3\pi/4$ and $5\pi/4$, the patterns can be represented by;

$$I_1 = I_0\left[1+\varphi\cos\left(\Delta\phi+\frac{\pi}{4}\right)\right] = I_0\left[1+\frac{\sqrt{2}}{2}\varphi(\cos\Delta\phi-\sin\Delta\phi)\right]$$

$$I_2 = I_0\left[1+\varphi\cos\left(\Delta\phi+\frac{3\pi}{4}\right)\right] = I_0\left[1+\frac{\sqrt{2}}{2}\varphi(-\cos\Delta\phi-\sin\Delta\phi)\right]$$

$$I_3 = I_0\left[1+\varphi\cos\left(\Delta\phi+\frac{5\pi}{4}\right)\right] = I_0\left[1+\frac{\sqrt{2}}{2}\varphi(-\cos\Delta\phi+\sin\Delta\phi)\right]$$

The phase is thus given by

$$\Delta\phi = \tan^{-1}\left(\frac{I_3-I_2}{I_1-I_2}\right) \qquad \text{Equation 2.11}$$

The five-frame technique was designed in an effort to minimise the possibility that the numerator and denominator could be zero. It, therefore, has less sensitivity to errors. This algorithm uses five frames which are 90 degrees apart, so the phase shifts are $-\pi$, $-\pi/2$, 0, $\pi/2$ and π. The five frames can be expressed as follows:

$$I_1 = I_0[1+\varphi\cos(\Delta\phi-\pi)] = I_0[1+\varphi\cos\Delta\phi]$$

$$I_2 = I_0\left[1+\varphi\cos\left(\Delta\phi-\frac{\pi}{2}\right)\right] = I_0[1+\varphi\sin\Delta\phi]$$

$$I_3 = I_0[1+\varphi\cos\Delta\phi]$$

$$I_4 = I_0\left[1+\varphi\cos\left(\Delta\phi+\frac{\pi}{2}\right)\right] = I_0[1-\varphi\sin\Delta\phi]$$

$$I_5 = I_0[1+\varphi\cos(\Delta\phi+\pi)] = I_0[1-\varphi\cos\Delta\phi]$$

The phase is, therefore, given by the expression:

$$\Delta\phi = \tan^{-1}\left(\frac{2(I_2 - I_4)}{2I_3 - I_5 - I_1}\right) \qquad \text{Equation 2.12}$$

Another class of algorithm used is the *(N+1)-frame technique*. This procedure has phase shifts $2\pi i/N$, similar to the synchronous detection method, with one extra frame having a 2π phase shift with respect to the initial frame, i.e. the last frame and the first frames are identical assuming zero phase shifting error. An example of this approach is the seven-frame version.

$$\Delta\phi = \tan^{-1}\left(\frac{\sqrt{3}(I_2 + I_3 - I_5 - I_6) + (I_7 - I_1)/\sqrt{3}}{-I_1 - I_2 + I_3 + 2I_4 + I_5 - I_6 - I_7}\right) \qquad \text{Equation 2.13}$$

Finally, an algorithm[8] was developed for large structures which could not be isolated from air turbulence and vibrations. It involves the use of many frames with random phase shifts between 0 and 2π. For each new frame the minimum and maximum intensity values can then be used to calculate I_0 at each point. In this case:

$$\Delta\phi = \cos^{-1}\left(\frac{I_i - I_0}{\varphi I_0}\right) \qquad \text{Equation 2.14}$$

where,

I_i = intensity data frame with phase shift α_i

$$I_0 = \frac{I_{max} + I_{min}}{2}$$

Due to the nature of arctangent calculations, the equations presented are sufficient only for modulo π calculation. In order to determine the phase modulo 2π, the signs of quantities proportional to $\sin\phi$ and $\cos\phi$ must be examined. Table 2.1[8] shows how the phase is determined.

Quadrant	$\sin\Delta\phi$	$\cos\Delta\phi$	Adjusted OPD	Adjusted Phase	Range of Phase Values
1	>0	>0	OPD	$\Delta\phi$	$0\rightarrow\pi/2$
2	>0	<0	$\lambda/2$-OPD	$\pi-\Delta\phi$	$\pi/2\rightarrow\pi$
3	<0	<0	OPD+$\lambda/2$	$\Delta\phi+\pi$	$\pi\rightarrow3\pi/2$
4	<0	>0	λ-OPD	$2\pi-\Delta\phi$	$3\pi/2\rightarrow2\pi$
1,2	>0	=0	$\lambda/4$	$\pi/2$	$\pi/2$
2,3	=0	<0	$\lambda/2$	π	π
3,4	<0	=0	$3\lambda/4$	$3\pi/2$	$3\pi/2$
4,1	=0	≥0	0	0	0

Table 2.1 Determination of phase, modulo 2π

The removal of phase ambiguities is generally called phase unwrapping, and is sometimes known as integrating the phase. Phase unwrapping yields an unwrapped phase map and this process will now be explored.

2.8 Phase Unwrapping

The phase shifting and Fourier transform techniques both yield a phase map which is referred to as a *wrapped* phase map. These maps must be unwrapped to gain absolute phase maps and this unwrapping process involves the removal of the 2π steps.

The key to this process is the accurate detection of the 2π phase jumps. The fundamental approach for processing a wrapped map involves sequentially scanning each horizontal line of the digital image to find abrupt phase changes between 2π and 0 or vice versa at the edge of the fringes. Once these jumps have been identified, an offset, which is a multiple of 2π, is either added or subtracted to the phase value of the appropriate pixel.

The technique relies on locating the fringe edges, therefore, any noise at the edges can seriously inhibit the process. Discontinuities hidden in the speckle noise can cause phase jumps to be neglected or offsets to be added/subtracted at incorrect locations. It is, therefore, important to ensure that all pixels in the input image contain information.

2.9 Summery

The various algorithms, which have traditionally been used for deformation testing, have been outlined in section 2.7.1. It can be seen that these methods cannot be used for high-speed motions, as they require the system to record the latter images whilst the object is moving. As a result an algorithm must be generated which will not have this requirement. The new algorithm must allow the recording of the data whilst the object is moving at relatively high speeds.

The system must allow for this by the design of software, which will carry out this data recording and store it for post process. It must also be portable, robust and as compact as possible. In chapter 3 the design of this system will be investigated as well as the methods used for its calibration and use with an application.

CHAPTER 3 EXPERIMENTAL

3.1 Set-up for ESPI Systems

1.1.1 3.1.1 In-Plane

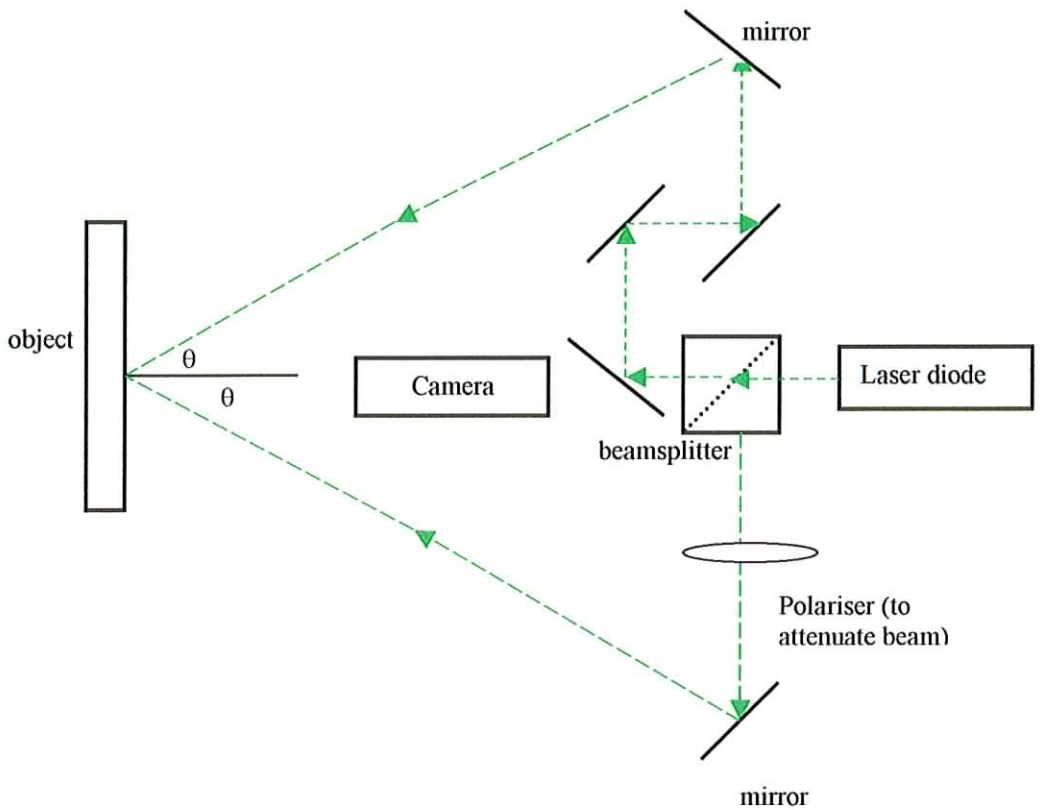

Figure 3.1 In-plane ESPI System

The objective of this part of the research was to set up, calibrate and test an in-plane ESPI system. After calibration the system was used for quantitative displacement measurement by using both the fringe counting and the phase shifting methods. In the system set up, as shown in figure 3.1, a beam is directed from a laser diode towards a beamsplitter where it is divided in two. These two beams are subsequently directed, using a system of mirrors, towards an optically rough surface.

Changing the injection current or the temperature of the action region of a laser diode can achieve direct frequency modulation of the laser diode[28]. This produces a variation in the wavelength thus yielding a phase change between the two beams in the interferometer, which is proportional to the given difference of the wavelength and the optical path difference. As the reference phase is dependant upon the optical path difference, the latter must be controlled carefully.

Each beam creates a speckle pattern on the surface and when these patterns interfere a resultant interference pattern is observed. When the object is displaced fringe patterns are formed by correlating the images taken before and after, as described in section 2.3. However for this to occur the system was first optimised to obtain maximum speckle contrast.

This optimisation means ensuring that the beams are of equal intensity, the same polarisation state and overlap as much as possible. The computer monitor displays a live image of the resultant pattern and this can be used to maximise overlap. A small polariser was placed in the set up as shown to control the intensity of one of the beams.

It is also important to control the speckle size as the best contrast occurs when the speckle size is in the order of a single pixel on the CCD array. Closing the camera aperture down increases the speckle size accordingly, as explained in Chapter 2. The maximum dynamic range (i.e. the ratio of the highest (brightest) signal which can be recorded to the lowest (darkest) signal) must be used in order to achieve maximum contrast. This is achieved by maximising the intensity by opening the camera aperture. However; there is a trade off between optimising the speckle size and maximising the intensity. It is also important not to open the aperture too much thus allowing too much light into the camera and saturating the image.

As mentioned in Chapter 2, ESPI differs from speckle photography in that it is a change in speckle intensity and not position that is correlated before and after the object is displaced. However, when the object moves the speckle do indeed displace but as long as this displacement is less that the size of a speckle, intensity correlation is still possible. However decorrelation occurs when the speckle moves too far i.e. if the motion of the speckle is greater than the speckle size. Assuming the speckle size is in the order of a pixel (10μm) then that is the maximum a speckle in the image plane can be displaced before total decorrelation occurs. The speckle size is controlled by the wavelength of the incident light as well as the imaging system used. To increase speckle size, the aperture size must be reduced, but this can prevent much of the laser light from reaching the CCD camera array.

When using continuous wave lasers, in the set ups, ESPI imposes very stringent stability requirements as rigid body motion between exposures must be kept to a fraction of the wavelength of the laser light. All components must be attached to the optical table as securely as possible. Microbench (Spindler & Hoyer) components were used along with magnetic stands to ensure the set up was as stable as possible. Environmental stability is also important and with this in mind thermal drift was minimised.

In the case of the out-of-plane systems the same criteria apply but in this system microbench was not used in order to improve flexibility. To maximise stability the laser diode was left on for long periods of time prior to commencement of all experiments. It was also important to remove from the optical table all pieces of apparatus that were to be manually controlled.

3.2 In-plane Calibrations

The system was calibrated using two imaging systems. Firstly, a conventional CCD camera was used at a recording rate of 25 frames per second. The same system was then calibrated using a high-speed camera, which can operate at speeds up to 4000 frames per second.

3.2.1 "Conventional" Camera

The object used was an optically rough disc mounted on a rotational stage. The stage was rotated through accurately defined angles and speed by a motorised micrometer with an optical encoder, which enabled the total translation to be displayed. The translation was then converted into a rotational angle. This allows for calculation of displacement at any point on the disc. Each 1.0 μm on the encoder corresponds to the object being rotated through 22.4 arc seconds. This disc is illustrated in figure 3.2.

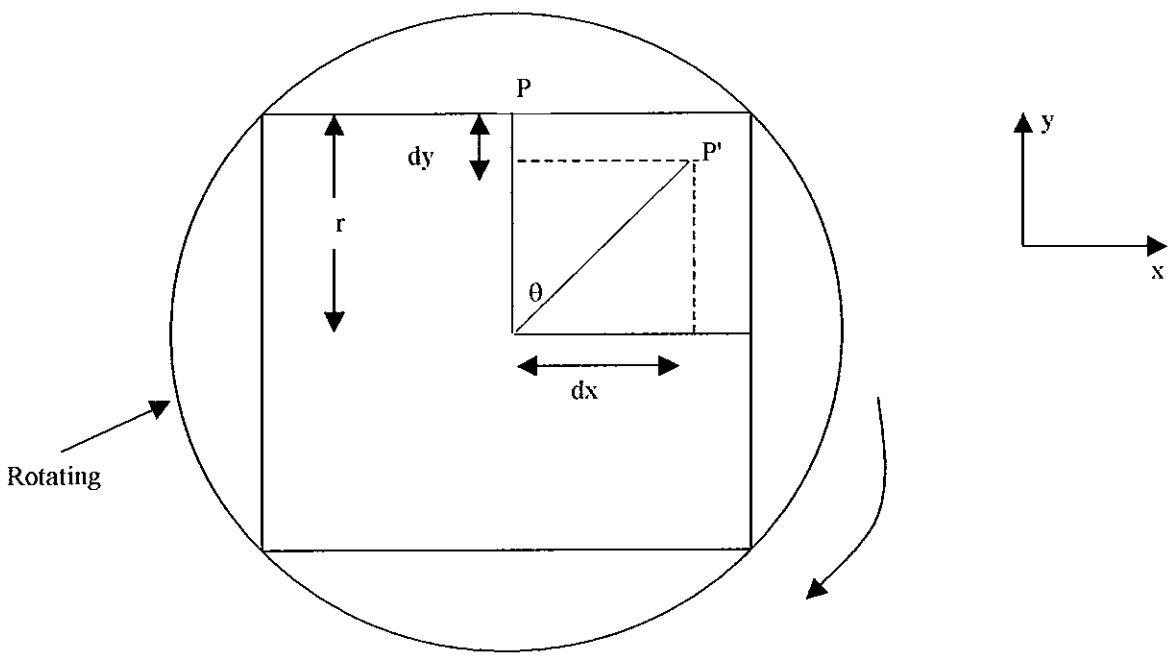

Figure 3.2 Rotating Disc

The in-plane system is only sensitive to displacements in the x direction so dx, the displacement in the x-direction, is found by looking at the motion of a point P to P'

After a clockwise rotation of θ the point P moves to P'. The displacement in the x direction is given by $dx = r\sin\theta$. The displacement in the y direction is given by $dy = r - r\cos\theta$.

In order to calibrate the set up the illumination angle θ, (see figure 3.1), was set at 19.5 degrees, measured trigonometrically. A known area of the rotational disc was illuminated and imaged.

The displacement in the x-direction was calculated at ten equally spaced points along the radius of the disc. A reference image was captured and then the disc rotated by a known amount and a subsequent image was then taken; this procedure was repeated for several rotations of the disc. Using, $x = r\sin\theta$, the displacements were calculated and these can be compared to the theoretical data calculated using equation 3.1. Since numerous tests are carried out to reduce the error in N, it is assumed that the major error in these calculations arises from the calculation of θ, for this reason the value for the illumination angle is corrected. If the beams were well collimated θ would not have a range of values, but that is not the circumstance here; in this case the value of θ varies slightly with distance from the centre, making the set up more sensitive to out of plane motion.

$$d = \frac{N\lambda}{2Sin\theta} \qquad \text{Equation 3.1}$$

3.2.2 High-Speed Camera

When the speed of rotation is increased the high-speed camera must be used in order to overcome the problem of decorrelation. A frequency doubled yttrium vanadate laser was used in conjunction with the conventional camera. When using the conventional camera the data is captured in near real time, however, when it is required that the system is used to measure movements at a high frequency this is not suitable as the camera can not record enough data. The software used, ESPItest©, limits the camera to acquiring images at a rate of 12 frames per second and thus much of the important potential data is lost. In order to capture as much of the movement of the object as possible a high-speed camera was used which can capture images at a rate of up to 4000 frames per second.

The ESPI system uses data acquisition hardware and frame grabber software to gather and save the data. As part of this research, an alternative program was designed which controls the data acquisition and analysis allowing the user to interpret it more easily. It allows the user control, via the front panel, of parameters such as the number of frames to be used, whether or not the software will carry out an array subtraction or an image subtraction as well as various filter functions such as stretch and contrast. The user can also use the front panel as illustrated in figure 3.3, to view data such as the current frame.

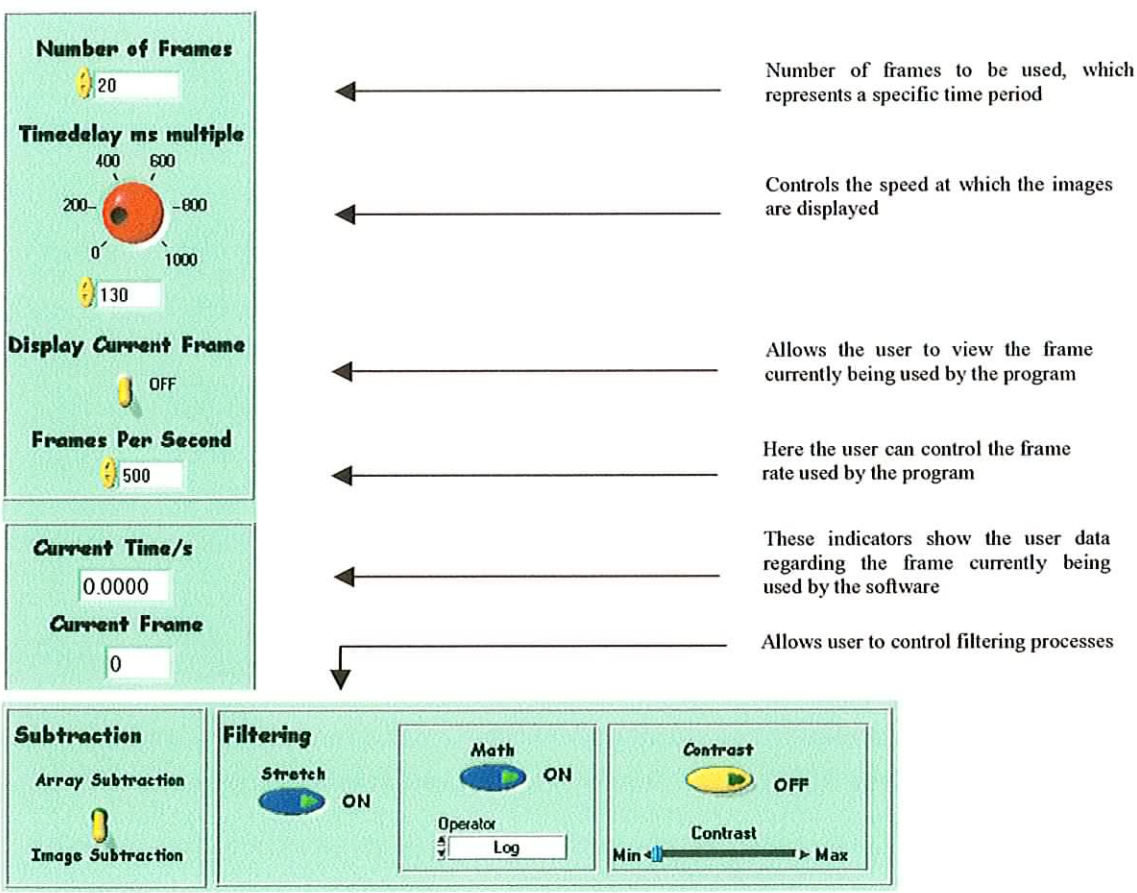

Figure 3.3 Front Panel of Program

When the conventional camera was replaced by the high-speed camera slight adjustments have to be made to the optical set up, including changing the lens. Also, due to the fact that the high-speed camera is recording at a high frame rate, its exposure time is reduced. This changed the set up slightly, and therefore, changed the angle of incidence leading to the need to recalibrate the system.

The apparatus was set up as shown in Figure 3.1. The high-speed camera software was run and the camera focused. A mark was placed on the centre of the disk and at a fixed distance from the centre of the disc (23mm). The laser was turned on and the set up manipulated until the two beams overlapped at equal intensities. The encoder was turned on at a known velocity and the camera program set to record; the data was then saved as bitmap images. The LabVIEW program was run and a speckle pattern was obtained and shown via the front panel. This was repeated for various "numbers of frames" and the resulting fringe patterns saved. This procedure was repeated for various velocities of the decoder and various recording rates of the camera. This technique is a post process method and this has some disadvantages; it is not possible to see the fringes forming in real time so it is not possible tell when decorrelation occurs. The process does not allow for stopping the procedure part way through; it must be completed and the results processed later.

If, for example, the encoder was set at a velocity of 40μm/s, the camera at a record rate of 250 frames per second and the LabVIEW program set at "15 frames" and r measured as 23mm, then,

$\frac{15\,frames}{250\,frames/s} = 0.06s$, this is the length of time between the first and last image

and at velocity of 40μm/s

$\Rightarrow (0.06)(40) = 2.4\ \mu m$

The encoder has a linear velocity of 2.4μm/s which corresponds to an angular velocity of the disc of 1.43×10^{-2} degrees per second,

As each micron on the encoder corresponds to 22.4 arc seconds ($6.22x10^{-3}$ degrees)

θ = (2.4μm) x (6.22×10^{-3} degrees) as shown in figure 3.2

Then, as with the conventional camera calculations,

$x = r.Sin\theta$

So,

$$Sin\theta = \frac{x}{0.023}$$

$$Sin\left[1.43\times10^{-2}\right] = \frac{x}{0.023}$$

$$x = 6.00\mu m$$

This calculated value was then compared to that measured by the ESPI system in order to calibrate the set up and this was repeated a numer of times at various speeds to show that the system was calibrated for any chosen speed.

3.2.3 Phase-Shift Calibrations

Phase fringes represent the phase change, in the range 0 and 2π. As previously stated changing the injection current of the action region of a laser diode can achieve direct frequency modulation of the laser diode. In order to use phase fringes to calibrate the system using the conventional camera, ESPItest© software was used. This software calculates the voltage required for a phase shift of 2π, and results in both wrapped and unwrapped patterns. ESPItest© was designed to correlate resultant speckle patterns in near real time[24]. The camera grabs images at a rate of 25 frames per second, however, the parameters of the software limit this to 12 frames. The program allows for the calculation of the 2π voltage by plotting the modulation of the laser at 16 chosen pixels.

The user can then choose one of these sinusoidal plots to calculate the voltage necessary to carry out the $\pi/2$ step required by the phase shifting algorithms.

For an in-plane system[1]

$$\Delta\phi = \frac{2dSin\theta}{\lambda} \times 2\pi$$

where,

$\Delta\phi$ represents the phase change

d is the displacement

θ is the angle of illumination

λ , wavelength

Since each phase fringe represents a phase shift of 2π

$$\Rightarrow N = \frac{2dSin\theta}{\lambda}$$

where N is the number of phase fringes for the displacement d.

3.2 Phase-Shifting Algorithms

LabVIEW programs were written and developed to carry out phase shifting, (Appendix 1). It was necessary to design and utilise algorithms that are able to cope with the high speed nature of the motions under investigation. The first one implemented the 4-Bucket algorithm calculating a value for ϕ for the object at rest. The second looked at calculation of the phase shift, which resulted after the displacement of the object ($\phi+\delta$). A final program was designed which calculates the resultant phase shift δ, by subtraction.

A step-by-step approach was used to ensure that the programs were working correctly. Firstly the programs were tested using ideal fringe patterns generated in LabVIEW. The patterns created were phase stepped by exactly $\pi/2$ and appeared as vertical fringes, they had a sinusoidal profile, were parallel and equally spaced. The phase shift was simulated by the user of the software by inputting the desired phase into the front panel of the software. Each image was then saved to the PC and subsequently used in the LabVIEW program designed to carry out the phase shifting algorithm. The wrapped phase map was then generated as illustrated in figure 3.6.

When it was confirmed that the program worked as anticipated the step-by-step approach was used with fringe patterns recorded from a Michelson interferometer to ensure that it could process actual experimental data. The software worked correctly thus allowing for the more noisy ESPI fringes to be used.

3.3.1 4-Bucket Algorithm

In order to obtain a phase map of the object, using this algorithm, four frames were recorded. These frames were taken at phase shifts of 0, $\pi/2$, π and $3\pi/2$ respectively, see equation 2.8. After the software was designed it was tested, and in order to do this a program was written which results in four "ideal" fringe patterns, i.e. perfect fringe patterns with no noise. The phase map which is shown in figure 3.4 illustrates the resulting phase map. These patterns were then used within the software to ensure it worked correctly.

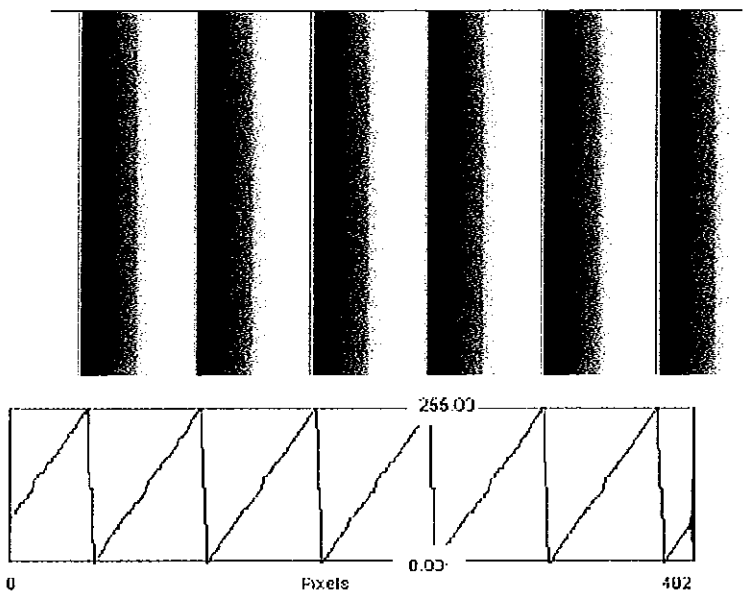

Figure 3.4 Data from software when using four "ideal" fringe patterns

Once the software was tested it was used in conjunction with experimental data. A Michelson interferometer was constructed to test the software using actual fringe patterns, see figure 3.5, but which are less noisy than speckle patterns. This was done to ensure that the software could work with actual experimental data and was not restricted to use with ideal patterns. If one of the mirrors in a Michelson interferometer is tilted, parallel fringes with a uniform spatial frequency across the field are observed. When a phase shift is introduced a phase map can be calculated; this map has an identical number of fringes to the pattern which is seen.

As states in section 3.2.3 the method of phase shifting, which was used initially, involved changing the laser wavelength, by modulating the laser current. Later a PZT was attached to one of the mirrors in the system and a controlled voltage placed across it. A mirror was tilted to form the fringes and then the PZT was used to phase shift. In this way the mirror could be displaced in a controlled manner.

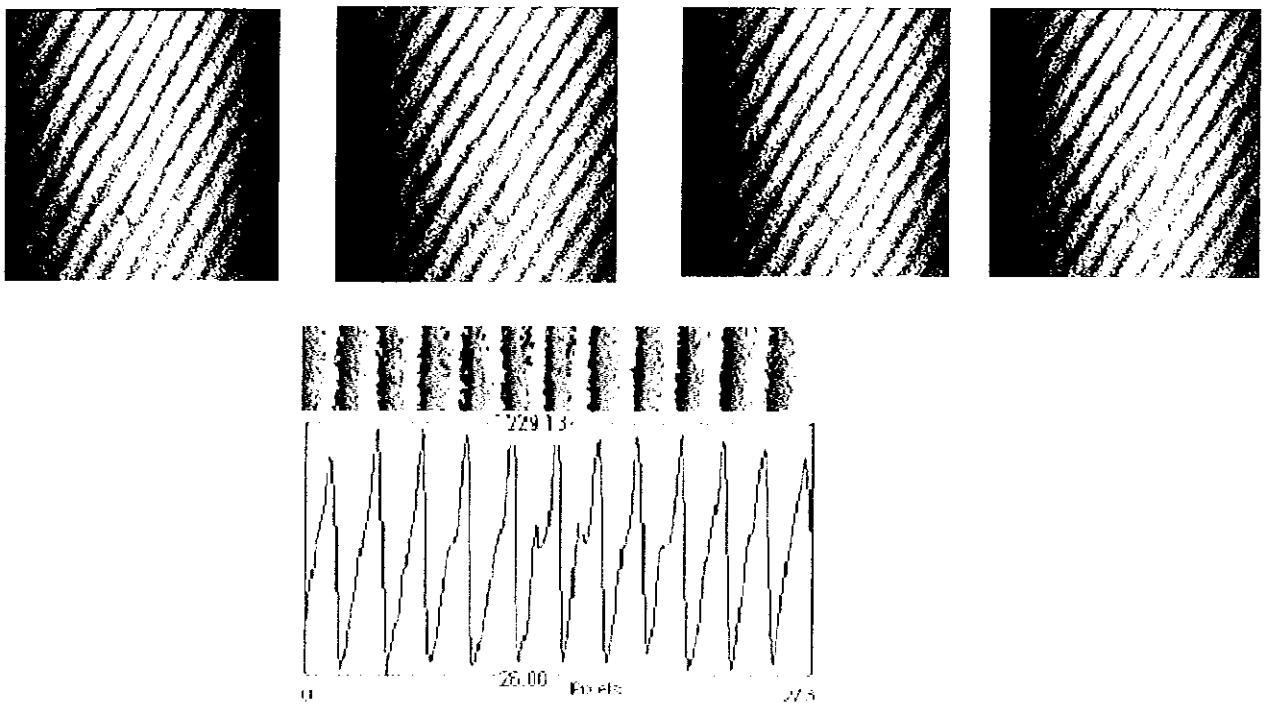

Figure 3.5 Data from software when using four Michelson fringe patterns

Figure 3.5 illustrates the resulting wrapped phase maps obtained from the Michelson set up. For illustration purposes a section through the sample, perpendicular to the fringes, has been taken and plotted horizontally. It can be seen that the desired ramped fringes have been obtained and as such it shows that this program was a viable way of obtaining phase data from an object at rest.

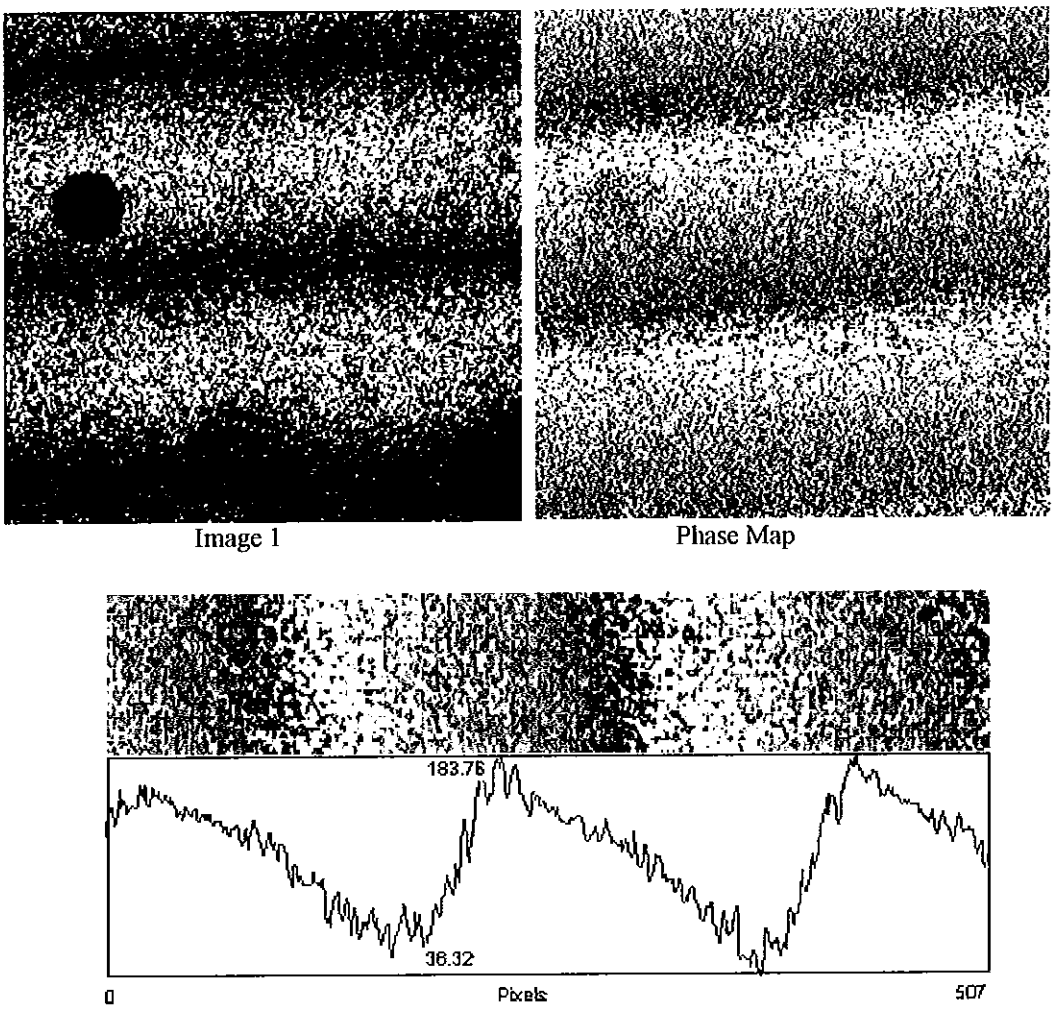

Figure 3.6 Data from software when using four ESPI patterns

In figure 3.6 the first image shows the displacement fringes as obtained through subtraction and rectification (correlation). The second image is the phase map obtained from the 4-bucket algorithm, which is caused from the same displacement, it can be seen that they correspond. The final image in this figure illustrates the graphical representation of the wrapped phase map, note that for illustration purposes a vertical section through the sample has been taken and plotted horizontally, again the ramped nature of the map can be clearly seen.

3.3.2 5-Frame Algorithm

The 4-Bucket method becomes redundant when measuring high frequency vibrations. This is due to the fact that acquiring the latter four images becomes impossible, as the object is moving. As a result another algorithm was designed to overcome this problem.

The intensity that results when two mutually coherent light beams superimpose is

$$I = I_1 + I_2 + \sqrt{I_1 I_2}\cos\Delta\phi$$

Several images are recorded for an object at rest with a constant phase shift between them. Looking at a case where the initial phase is $\phi+\delta$, where ϕ is the random speckle phase and $-\delta$ the subsequent phase change at x,y due to the motion of the object[24].

The initial frames recorded, while the object is at rest can be represented by

$$I_0 = I_1 + I_2 + 2\sqrt{I_1 I_2}\cos(\Delta\phi + \delta)$$
$$I_{\pi/2} = I_1 + I_2 + 2\sqrt{I_1 I_2}\cos\left(\Delta\phi + \delta + \pi/2\right)$$
$$I_{\pi} = I_1 + I_2 + 2\sqrt{I_1 I_2}\cos(\Delta\phi + \delta + \pi)$$
$$I_{3\pi/2} = I_1 + I_2 + 2\sqrt{I_1 I_2}\cos\left(\Delta\phi + \delta + 3\pi/2\right)$$

The object is then set in motion and several frames recorded, any one of those frames can then be used as I', which is represented as follows

$$I' = I_1 + I_2 + 2\sqrt{I_1 I_2}\cos\phi$$

Each of the previous equations are then subtracted from this, which in turn gives

$$I_1 = 2\sqrt{I_1 I_2}\left[\cos\phi - \cos(\Delta\phi + \delta)\right]$$
$$I_2 = 2\sqrt{I_1 I_2}\left[\cos\phi - \cos\left(\Delta\phi + \delta + \pi/2\right)\right]$$
$$I_3 = 2\sqrt{I_1 I_2}\left[\cos\phi - \cos(\Delta\phi + \delta + \pi)\right]$$
$$I_4 = 2\sqrt{I_1 I_2}\left[\cos\phi - \cos\left(\Delta\phi + \delta + 3\pi/2\right)\right]$$

$$\frac{I_4 - I_2}{I_3 - I_1} = \tan(\Delta\phi + \delta)$$

So this 5-image algorithm uses the same four phase-stepped images as its predecessor, however, it only requires one image, I', to be recorded after the object begins to move. The high-speed camera grabs up to 4000 images per second. Any one of these can be used as I' in the algorithm giving values for δ at every point, at any instant of the motion of the object as long as decorrelation does not occur. Since the 4-Bucket algorithm has been used to calculate the value for ϕ a value for σ can now be found.

As with the previous algorithm this program was tested using "ideal" fringe patterns generated by LabVIEW, see figure 3.7.

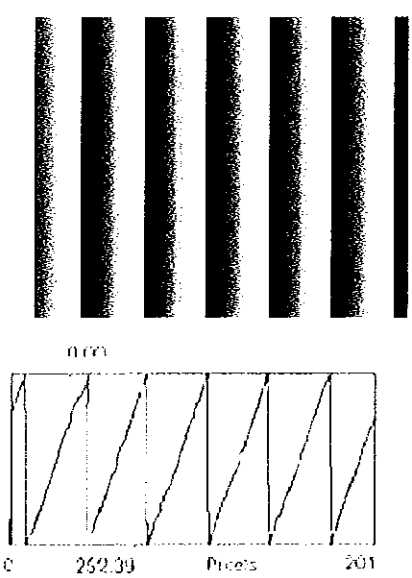

Figure 3.7 Data from software when using five "ideal" fringe patterns

Again, it can be concluded that, as the software obtained wrapped phase maps, it is reliable and so can be used in conjunction with experimental data from the Michelson interferometer as shown in figure 3.8.

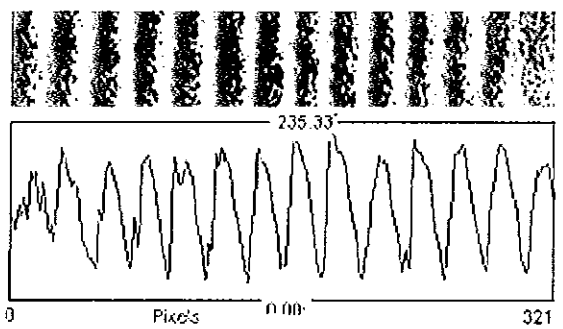

Figure 3.8 Data from software when using five Michelson fringe patterns

As with the 4-Bucket algorithm, it has been shown that this program is a feasible way of obtaining phase data from an object. The set up can now be used with ESPI patterns.

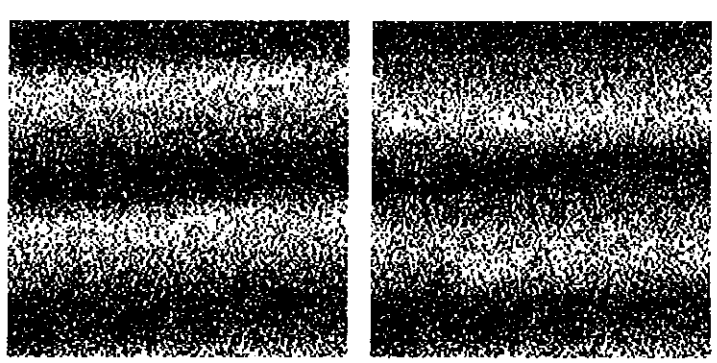

4-Bucket Algorithm (twice) 5-Frame Algorithm

Figure 3.9 Data from software when using five ESPI patterns

The phase maps illustrated in figure 3.9 were obtained when using ESPI patterns. The first image illustrates what was achieved when the four-bucket algorithm was used before and after the motion of the object and the resulting patterns subtracted. The second image shows the result of the 5-image algorithm when recording at a relatively high frame rate of 1000 frames per second. Both methods result in a wrapped phase map which can then be used to calculate the motion of the object under investigation.

3.4 Phase-Shifting using a PZT

All of the experimental data above was gathered using the modulation of the laser diode to control the phase steps. This method, however, is not ideal for automation in LabVIEW as calculating the required modulation of the laser diode is far more complicated a method to automate than the motion of a PZT through the modulation of its voltage supply.

Using the laser diode to modulate the phase only works when the path lengths are not matched, in fact the larger the difference in path length the easier it is to modulate. The PZT however, upon which one of the mirrors in the system was mounted, was used to phase shift because not only is this new set up compatible with the software of the high-speed camera but it also used a higher power laser. The laser diode has an output power in the region of 150mW whereas the argon ion laser has an output of 5W. This higher power is required to increase the intensity so as to gain a reading from the CCD camera as its exposure time is significantly reduced.

Figure 3.10 illustrates the flow diagram for the automated approach.

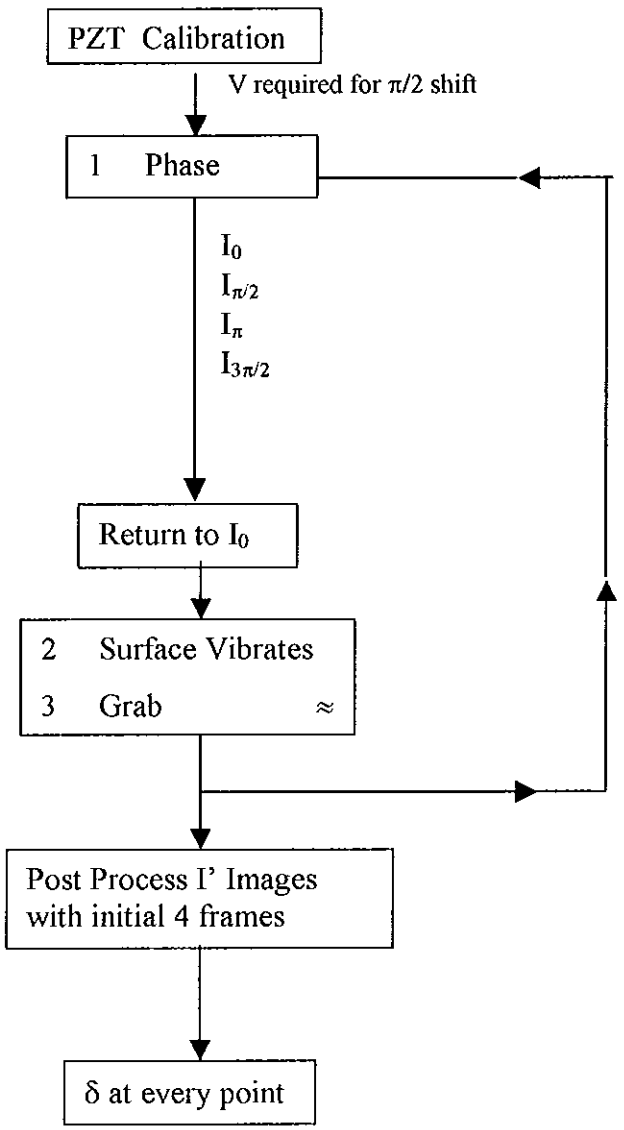

Figure 3.10 The flow diagram for phase shifting

3.4.1 PZT Calibration

A LabVIEW program, see figure 3.11, was written for purpose of calibrating the PZT in order to use it to phase shift. The program requires the user to enter parameters such as the number of frames to be processed, the increment by which the voltage will be increased and the coordinates of the pixels under investigation. Once communication has been established the program proceeds to increase the voltage across the PZT by the set increment, see Appendix 1 for the block diagram of the software. As the PZT is moved the frames are displayed on the monitor. For each frame the program calculates the intensity at each of the given coordinates and the program plots the intensity of the pixel under investigation against the frame number.

Once the graphs are obtained they are each sent to a peak detector. This detector finds any peak that is 25% of the magnitude of the maximum peak. The locations of these peaks are then used to calculate the voltage required for a phase shift of $\pi/2$. The PZT is now calibrated for use in any interferometric system.

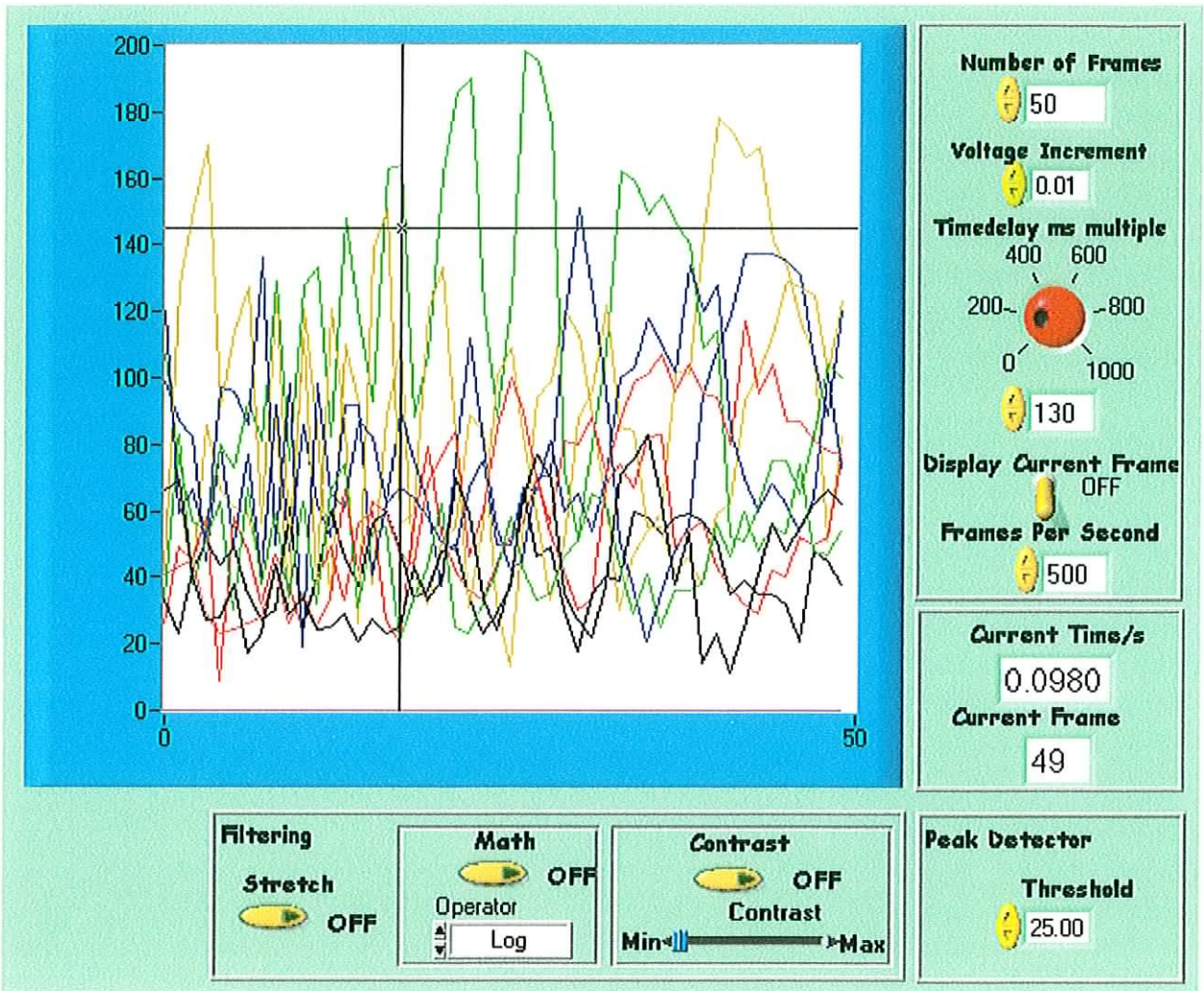

Figure 3.11 Front panel of calibration software

At first glance figure 3.11 seems to be a set of random plots. As stated in section 3.2.3 ESPItest© plots the modulation of 16 random pixels and the user utilises this information to calculate the step. Similarly, the LabVIEW program plots the intensity of 12 pixels, coordinates controlled by the user, to generate the graphs illustrated in figure 3.13. The reason why so many pixels are used comes from the fact that there are invariably some bad or dead pixels in the pattern and it is important to ensure that one of these is not used in the subsequent calculations.

Using many plots allows the user to disregard any which do not modulate, ESPItest© uses a similar technique. However, when using ESPItest© the user must choose one of the graphs and click on the peaks of the sinusoid. In the LabVIEW program the software uses a peak detector to calculate the $\pi/2$ value of the modulation for the user, which means that the program is capable of locating peaks within a given graph and to use its position in a subsequent calculation. All the user needs to do is choose which plot to take the value from. The program also allows the user to set a threshold value for the detection of the peaks within the sinusoids. Once this value is calculated the algorithms can be used.

Once the voltage required for a phase shift of $\pi/2$ is known the set up can be used to carry out phase shifting measurements. Figure 3.12 illustrates some of the patterns from this method.

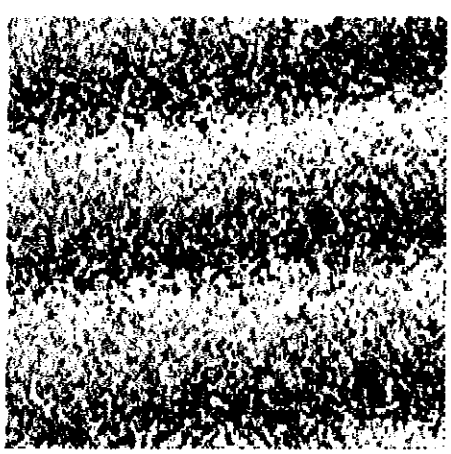

250 frames/sec
2.0μm movement

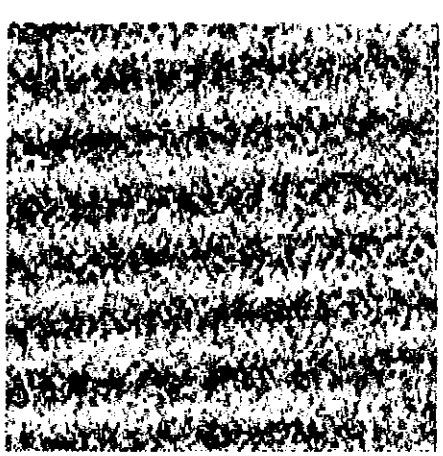

500 frames/sec
5.0 μm movement

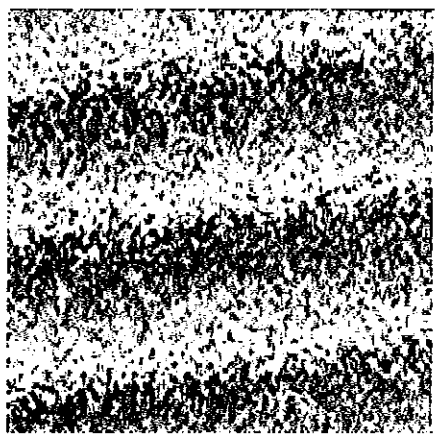

1000 frames/sec
3.0 μm movement

Figure 3.12 Wrapped Phase Maps resulting from 5-frames technique

3.4.2 Comparison between 4-Bucket and 5-Frame techniques

The calibration process which was used previously (see section 3.2.3) is again carried out, however, this time with wrapped patterns obtained from both the 4-bucket and the 5-frame algorithms. In this way the two methods can be compared. In the following chapter table 4.5 illustrates the fact that the errors calculated using the 5-frame technique are less than those found with the 4-bucket algorithm due to the fact that only 5 frames must be captured as opposed to the 8 required for the 4-bucket method.

3.5 Application

An out-of-plane ESPI system was built in order to view the radial expansion of a clamped cylinder which is pumped with compressed air and hence expands and contracts rapidly. The pressure in the cylinder can be varied between zero and 2.5 bar in steps of 0.1 bar. The rapid nature of the expansion and contraction of the cylinder leads to the neccessity of using the high-speed camera to capture the displacement.

The set up is shown in figure 3.13. Using a hologram within the system is not necessary, however, it does mean that the optical alignment difficulties are minimised. The hologram itself, acts like a beam combiner thus there is no need for a separate beam-combining device as with conventional ESPI. Also there is an added benefit of obtaining very good fringes with good contrast, which is of great advantage when using the system for phase shifting.

The value for the voltage required for a phase shift of $\pi/2$ is calculated as described in section 3.4.1. The four phase stepped images are recorded and saved to the PC. Since it was not possible to use the PZT in this set up the phase shifting was carried out using the modulation of the laser diode. After the initial four images were recorded in that way the cylinder was pumped full of air and the camera set to record the images at a frame rate of up to 4000 frames per second. Any one of these images could then be used as the fifth image in the 5-frame algorithm thus allowing for measurement of displacement of any point within the image at virtually any instant in the motion of the cylinder.

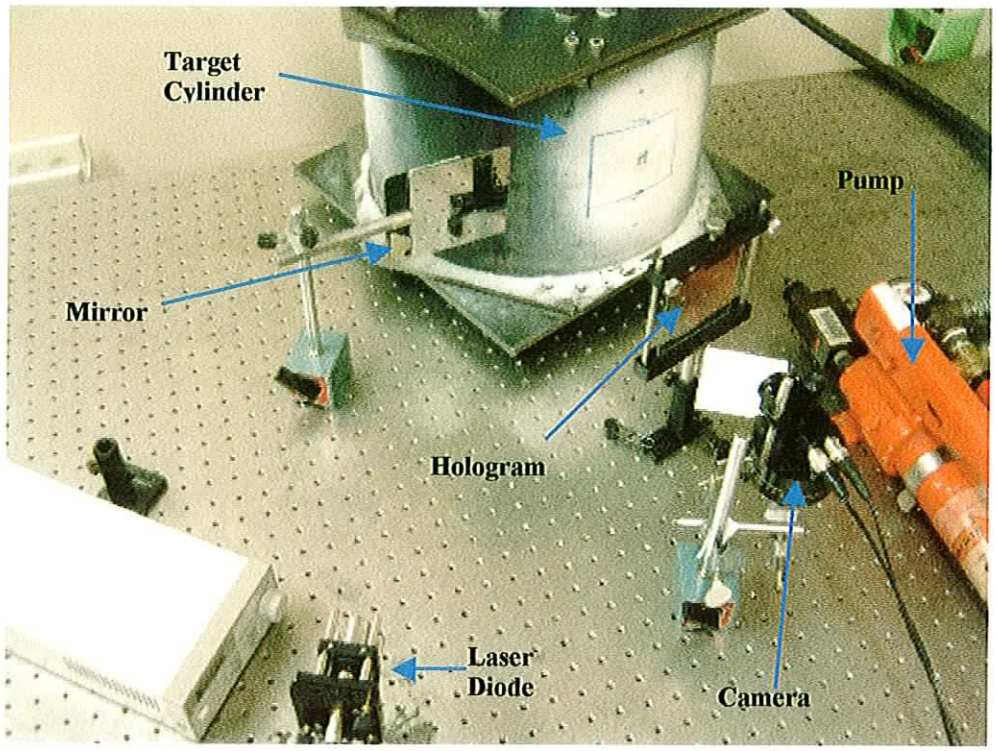

Figure 3.13 Out-of-plane set up

Some examples of the wrapped phase maps obtained from the cylinder are shown in figure 3.14. They illustrate the concentric fringe patterns obtained from the rapid displacement of the cylinder. This system also has an advantage over conventional ESPI because the framing rates are so high that low frequency thermal and mechanical vibrations do not have such a great effect. The system also allows for calculation of wrapped phase maps and their addition to achieve a complete wrapped phase map. By calculating the phase maps for small changes and adding them together one can calculate a phase map for a large change thus decreasing errors due to decorrelation.

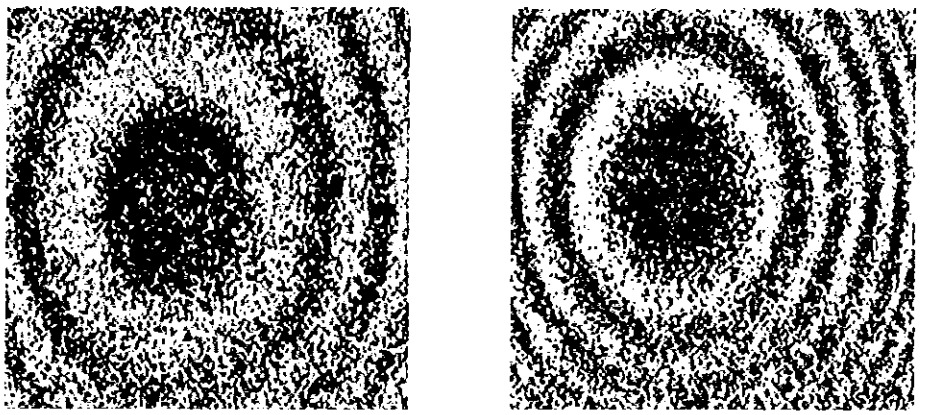

Figure 3.14 Resultant Wrapped Phase Maps

The first image shown in figure 3.14 illustrates the formation of a few fringes after a small time period had elapsed. The second image shows that more fringes are formed as the compressed air leaves the cylinder. It can be seen that as the cylinder relaxed the fringes became more closely spaced. In this way the contraction of the cylinder can be observed qualitatively and can be quantitatively calculated. The fringes are seen to move into or out from the centre of the pattern depending on whether the cylinder is being expanded or deflated.

The values of relaxation of the cylinder obtained can be compared to that calculated from the following[29]:

$$E = \frac{R_1^2}{(R_2^2 - R_1^2)}(2-\nu)\frac{P}{\varepsilon_t}$$

E = modulus of elasticity = 3.3 GN

R_1 = Internal radius of the cylinder = 15.6 cm

R_2 = External radius of the cylinder = 18.6 cm

θ = Angle between illumination and observation direction = 18.2°

P = Applied pressure

ν = Poisson's ratio = 0.333

$$\varepsilon_t = \frac{\Delta R_2}{R_2}, \text{ where } \Delta R_2 = d = \frac{N\lambda}{(1+\cos\theta)}$$

θ = Angle between illumination and observation direction = 18.2°

In this way it can be seen if the relaxation measured by the ESPI system was of the order of what was expected.

The algorithm, which was previously tested and used in a high-speed ESPI system, has now been used to test an object in an industrial type situation which was moving at speeds beyond what conventional ESPI systems could measure.

CHAPTER 4 RESULTS

4.1 In-plane Calibrations

4.1.1 Conventional Camera

The data in this section were gathered when calibrating the in-plane system using the conventional camera. The results shown were taken from the displacement of a disc whose motion is controlled and can be compared with the experimental data. The experimental data is then corrected for errors in the measurement of the angle of illumination. By looking at the modeled and experimental cases and calculating the value required for θ, these values are then plotted as shown below in figure 4.1. The accuracy of the method can then be measured by calculating the errors in the graph.

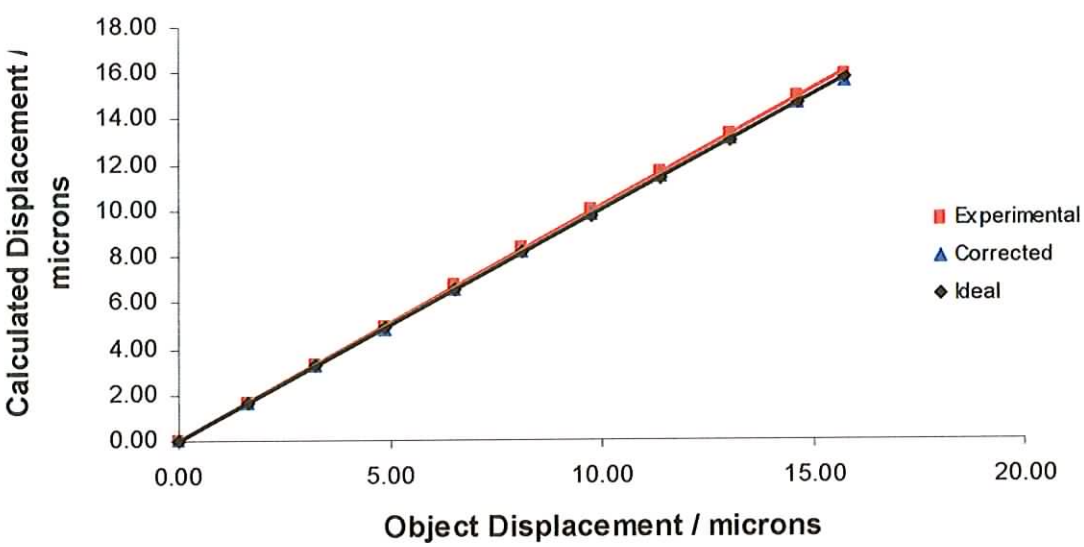

Figure 4.1 Graph of the x-displacement as a function of distance from center of disc

Using the slopes of the lines this set of experimental data has a percentage difference of 1.56%. However, when the data is corrected for the error in the angle then this difference is reduced to 0.22%. Also, in the experimental case the standard deviation of the displacement is 5.41 and the deviation in the corrected case is 5.32, implying that the corrected case varies less from the ideal case.

In all of the graphs illustrated in this chapter a linear regression technique was used. The legend in the above graph shows the plots of the experimental data, the data corrected for any error in θ and the ideal situation. Due to the fact that the beams were not collimated the value of θ depends on which point on the object is considered and this results in the corrected lines on the graph diverging more and more from the ideal as the extremities of the disc are reached this problem was discussed in chapter 3.

4.1.2 High-Speed Camera

In these trials the velocity of the rotating disc is increased greatly thus making conventional ESPI redundant and leading to the use of the high-speed camera. This procedure was carried out many times, see appendix 2, in order to ensure that the technique used remained suitable for all speeds.

Camera capturing images at a rate of 125 frames/s

The encoder has a linear velocity of 10μm/s which corresponds to an angular velocity of the disc of 6.22×10^{-2} degrees per second.

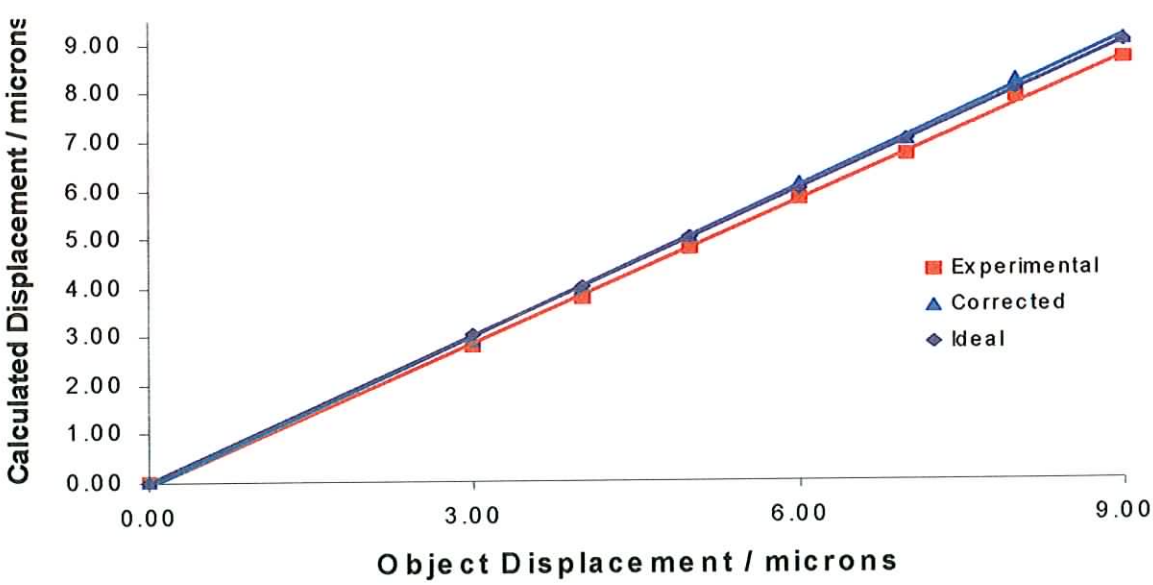

Figure 4.2 x-displacement as a function of distance from center of disc using high-speed camera

This graph clearly shows the divergence of the experimental data from the ideal as the distance from the center of the disc is increased. From this point on, only the corrected data will be shown as all of the subsequent graphs will be corrected for θ.

Camera capturing images at a rate of 125 frames/s

Encoder linear velocity of 15μm/s, angular velocity 9.33×10^{-2} degrees per second

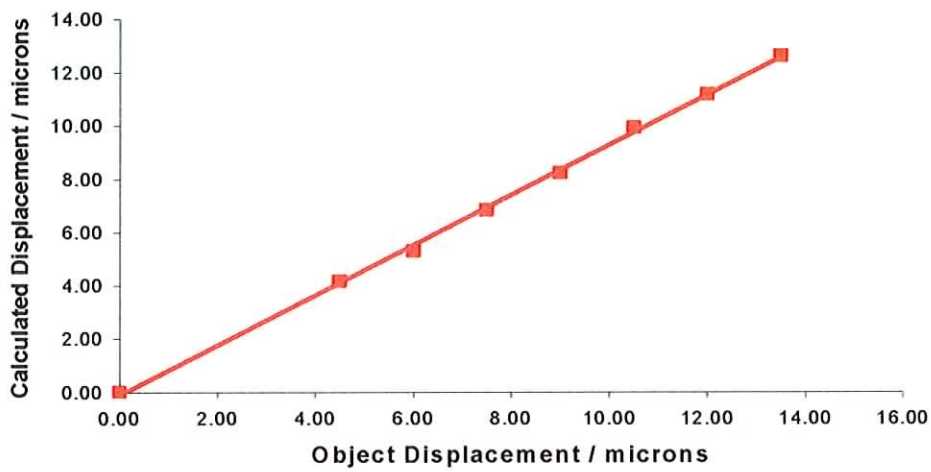

Figure 4.3 x-displacement as a function of distance from center of disc using high-speed camera

Camera capturing images at a rate of 250 frames/s

Encoder linear velocity of 40μm/s, angular velocity 24.88×10^{-2} degrees per second

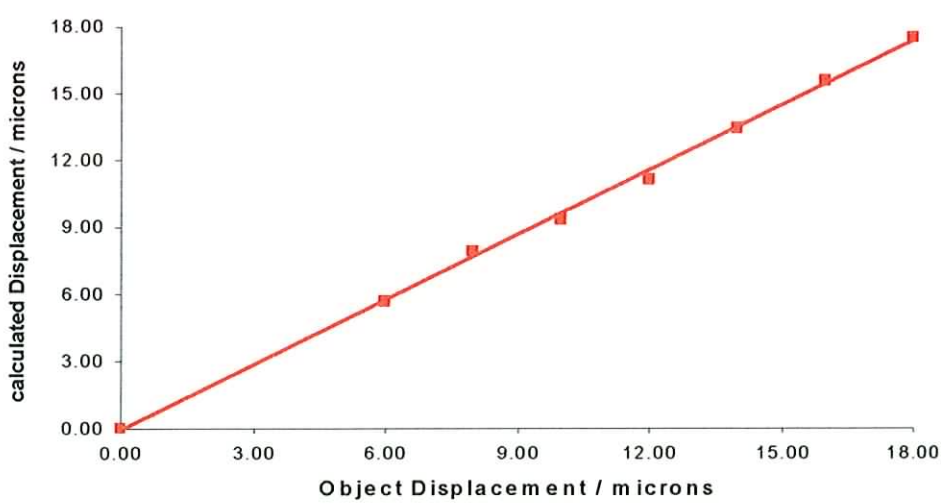

Figure 4.4 x-displacement as a function of distance from center of disc using high-speed camera

Camera capturing images at a rate of 1000 frames/s

Encoder linear velocity of 30μm/s, angular velocity 18.66×10^{-2} degrees per second

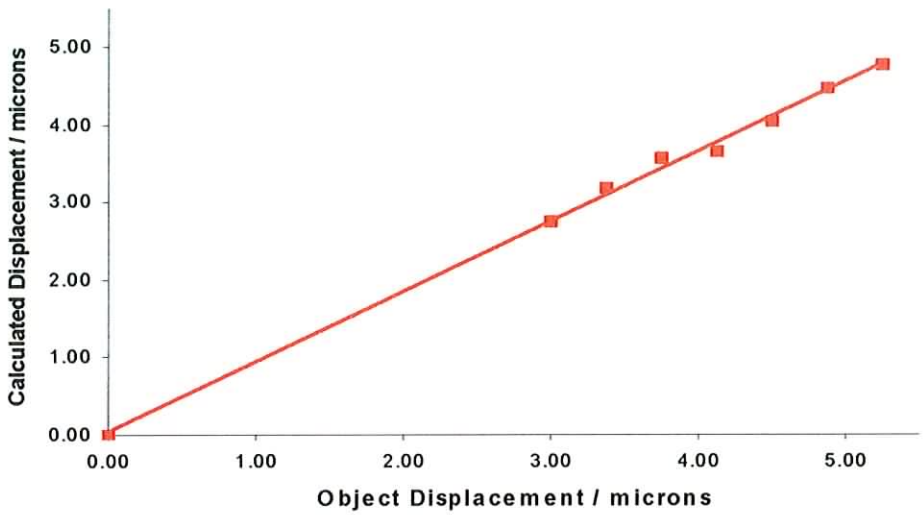

Figure 4.5 x-displacement as a function of distance from center of disc using high-speed camera

Camera capturing images at a rate of 1000 frames/s

Encoder linear velocity of 40μm/s, angular velocity 24.88×10^{-2} degrees per second

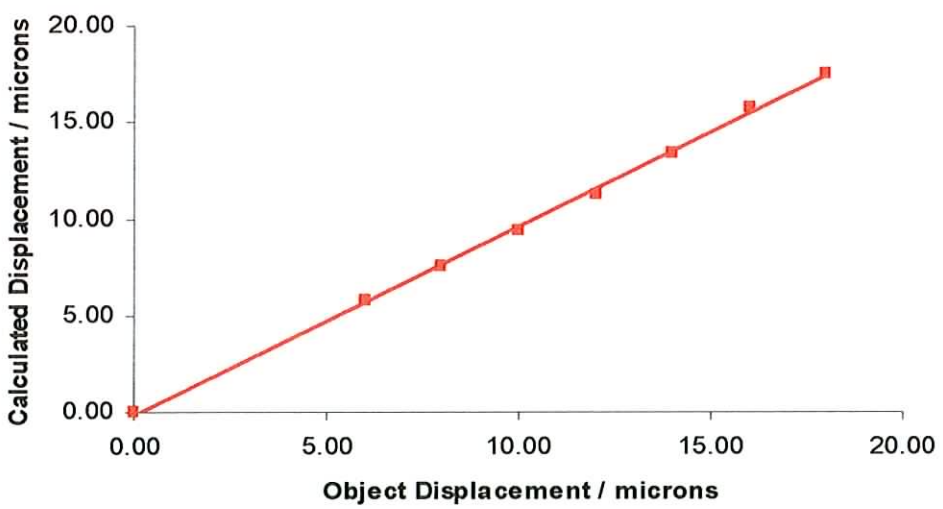

Figure 4.6 x-displacement as a function of distance from center of disc using high-speed camera

Camera capturing images at a rate of 1000 frames/s

Encoder linear velocity of 45μm/s, angular velocity 27.99×10^{-2} degrees per second

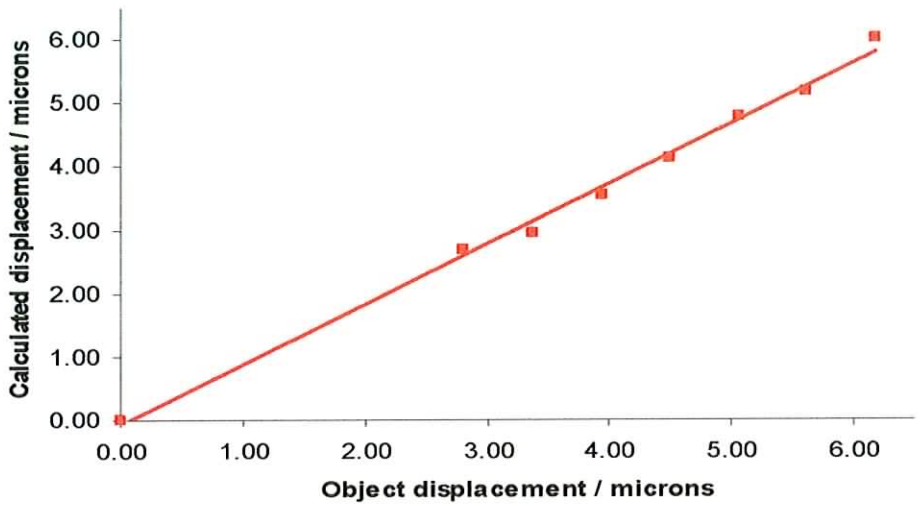

Figure 4.7 x-displacement as a function of distance from center of disc using high-speed camera

The graphs in figure 4.7 show some examples of the various velocities of the disc as well as the various frame rates used to calibrate the system at high speeds. The graphs are as expected in that they are linear and diverge from the ideal case as the disc moves.

Table 4.1 illustrates the data recorded for the high-speed calibrations. The procedure was carried out for various speeds and the calculations carried out in the same way as with the conventional camera.

Table 4.1

	Experimental		Corrected	
Frame Speed and Encoder Displacement	**% error**	**Standard Deviation**	**% error**	**Standard Deviation**
125 frames/s 10μm	2.81	2.84	1.84	2.78
125 frames/s 15μm	6.09	4.19	1.60	4.11
250 frames/s 40μm	3.20	5.63	1.17	5.55
1000 frames/s 30μm	6.37	1.57	1.35	1.52
1000 frames/s 40μm	2.79	5.57	2.65	5.55
1000 frames/s 45μm	5.22	1.91	2.52	1.84

It has been shown here that the system has been calibrated for use with the high-speed camera. The calibration was carried out at various velocities to show that once the set up is calibrated the system can be used at all of the available frame rates. The graphs show that the error does not change significantly when the velocity is increased, again showing that the system is now set up to be used at all frame rates. It is concluded that the system can now be used to calculate unknown displacements in this way. When capturing images at higher frame rates the area under investigation is smaller than at lower rates due to the need to maximize the power output of the laser and memory restrictions, this accounts for slightly less accurate results at the higher speeds.

As stated in chapter 3 the measurement of the displacement is more accurate when using phase shifting. This premise will now be explored by calibrating the system again but now using wrapped phase maps rather than the displacement fringes used in this section.

4.2 Phase-Shifting Calibrations

The calibration process used in the above examples of the data gathered was used again, however, in this case, phase shifting was used to generate the fringes under investigation.

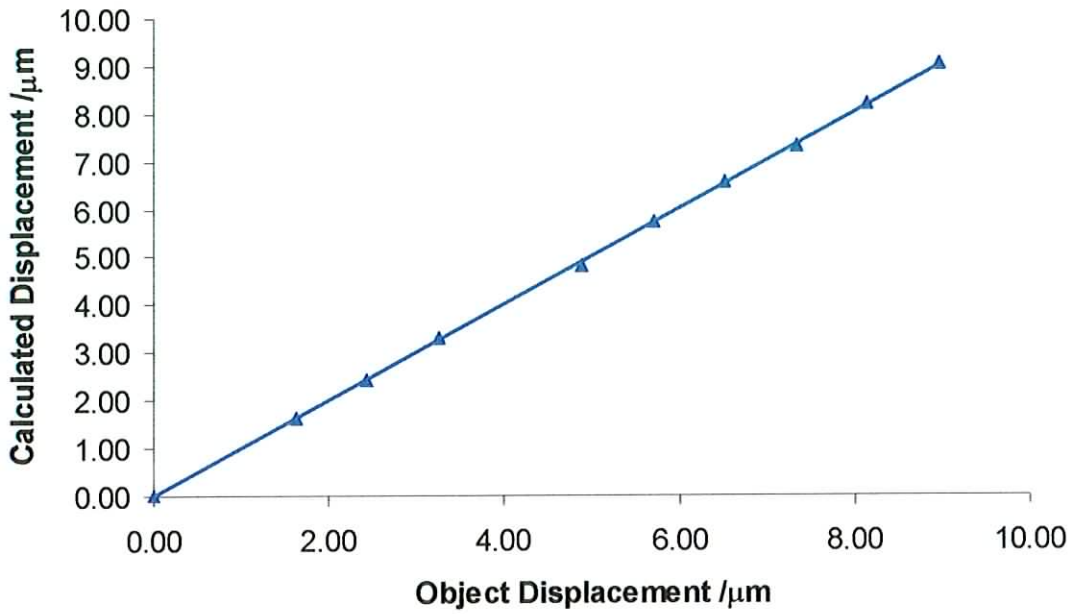

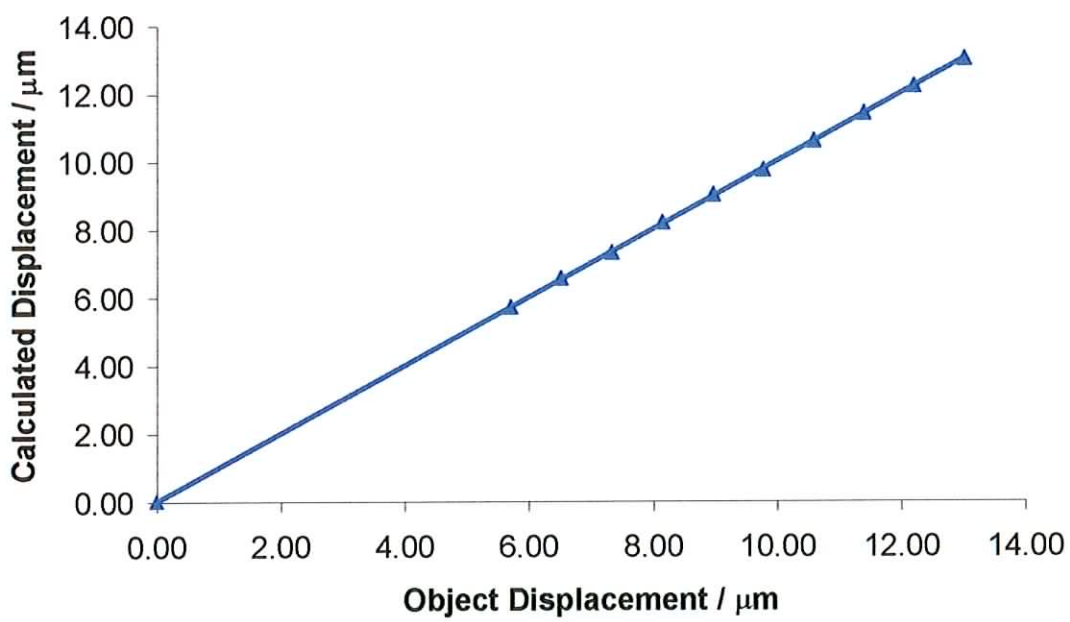

Figure 4.8 Calibration Curves resulting from phase fringes

Table 4.2

	Experimental		Corrected	
Frame Speed and Encoder Displacement	**% error**	**Standard Deviation**	**% error**	**Standard Deviation**
Trial 1	0.83	3.10	0.21	2.98
Trial 2	0.67	3.71	0.16	3.66

The above procedures show that this method for the observation and calculation of displacements is an accurate technique, as it results in an accurate calculation of the displacement of the disc. It can be seen that the percentage errors are very low and that, as expected, it is a more accurate method than using displacement fringes. This is because phase maps are ramps whereas displacement maps are sinusoids, thus making them a more accurate means of measurement. Therefore, it is concluded that this method can be used to calculate displacements.

Since the phase steps will be generated using a PZT, the PZT must also be calibrated.

4.3 PZT Calibration

For these trials the high-speed camera was set up and the PZT attached to one of the mirrors in the set up. The argon ion laser was used in order to utilise its higher power output, this higher power is required to increase the intensity so as to gain a reading from the CCD camera when recording at high frame rates. One of the mirrors was tilted in order to obtain the fringe pattern and then a voltage placed across the PZT in order to phase shift the fringes. This movement of the pattern was recorded at different framing rates and the generated speckle patterns, numbering in hundreds, captured. These patterns were then processed using the LabVIEW software outlined in section 3.4.1 and their intensities plotted. This process was used to calculate the voltage across the PZT required for a phase shift of $\pi/2$ in each case. Once this value was known the PZT could be used to perform the required calibrated phase steps needed to generate the fringe patterns used in algorithms.

Figure 4.4 illustrates some examples of the wrapped phase maps obtained using this method.

Frame Rate Movement	Resulting Wrapped Phase Maps	Plot of horizontal line taken through sample
250 frames/sec 2.0μm movement	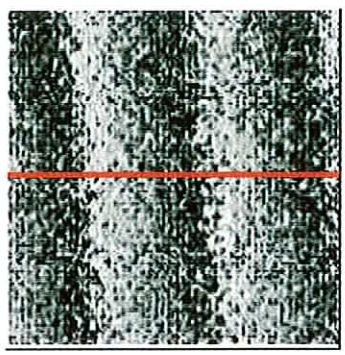	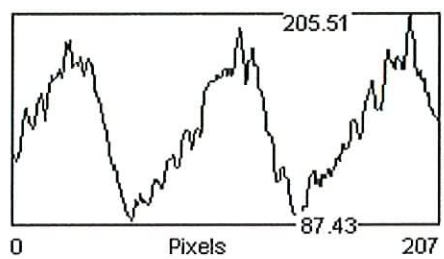
500 frames/sec 5.0 μm movement	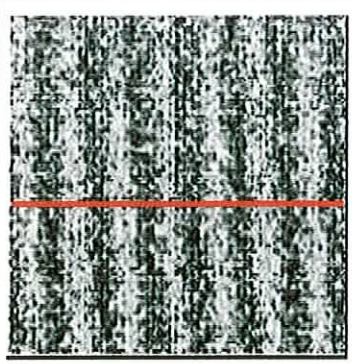	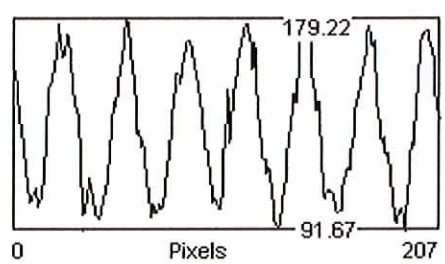
1000 frames/sec 3.0 μm movement	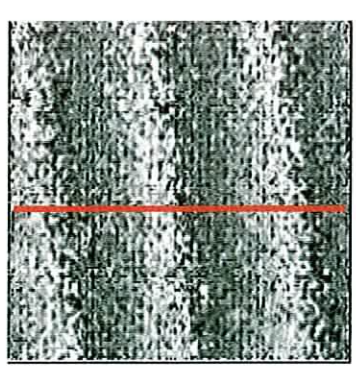	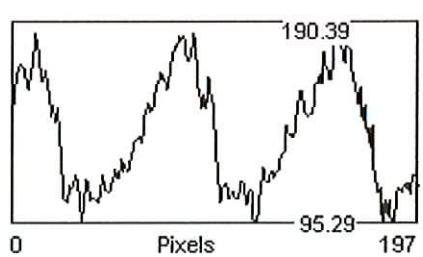

Figure 4.4 Example wrapped phase maps resulting from 5-frame technique

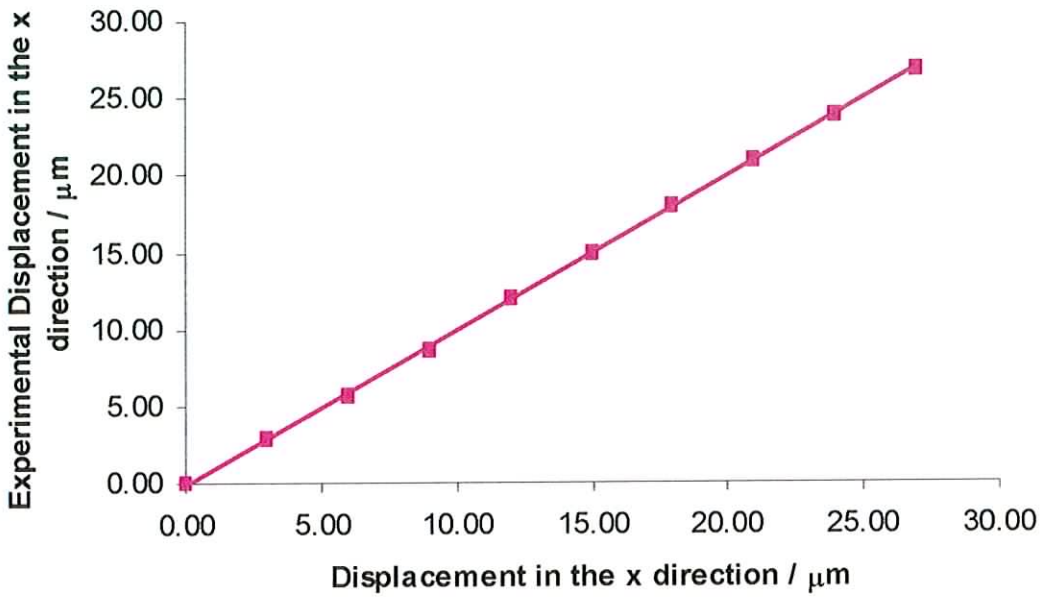

Figure 4.4 PZT Calibration Results

This procedure was carried out several times. One trial is illustrated in figure 4.4 and shows that the value calculated for the voltage required for a phase shift of $\pi/2$ is accurate. Since the expected displacement is calculated using these maps it can be concluded that the 5-frame technique has been successful in the generation of the required wrapped phase maps. It has been shown that the calculated phase step was correct and so it can be said that the PZT calibration was accurate.

4.3.1 Comparison of 4-Bucket and 5-Frame techniques

Each of these tests were carried out several times; see appendix 2 for tabular form of the data. The graphs within figure 4.5 illustrate experimental data which has been corrected as shown in section 3.3.

125 frames/sec

2.2μm movement

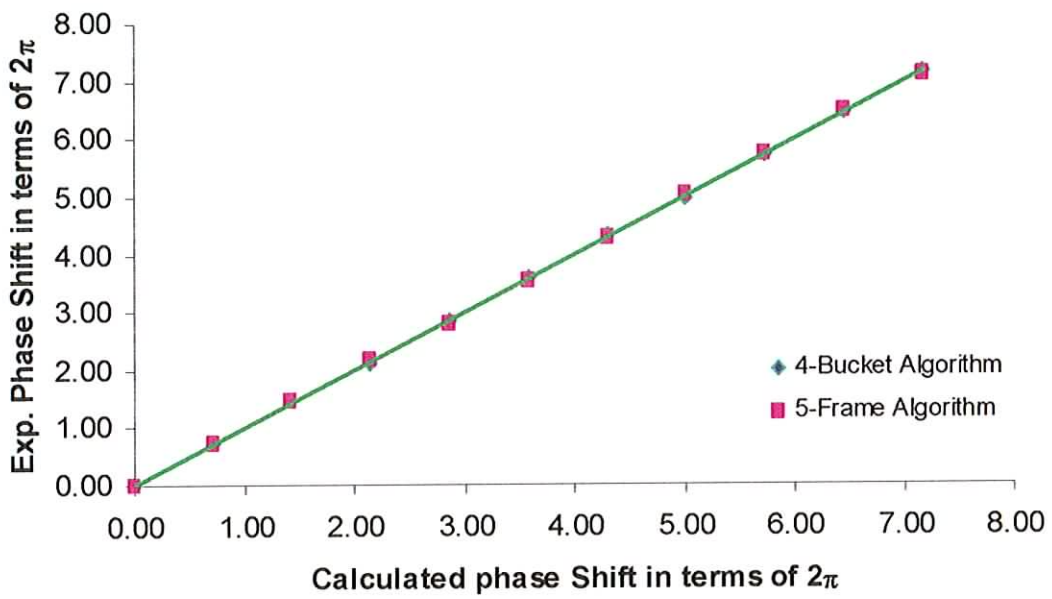

125 frames/sec

4.0μm movement

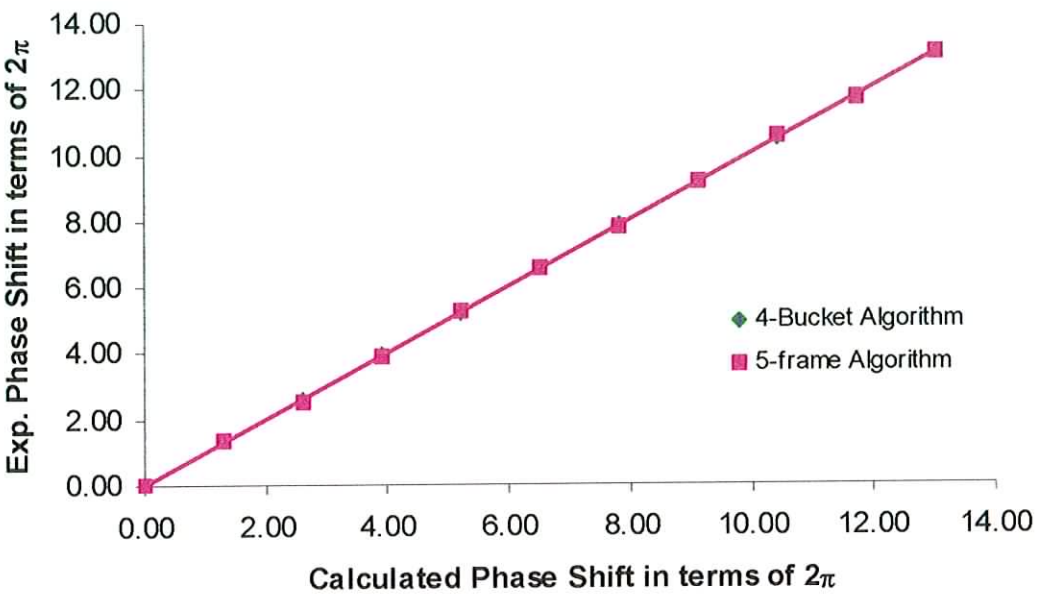

250 frames/sec

2.0μm movement

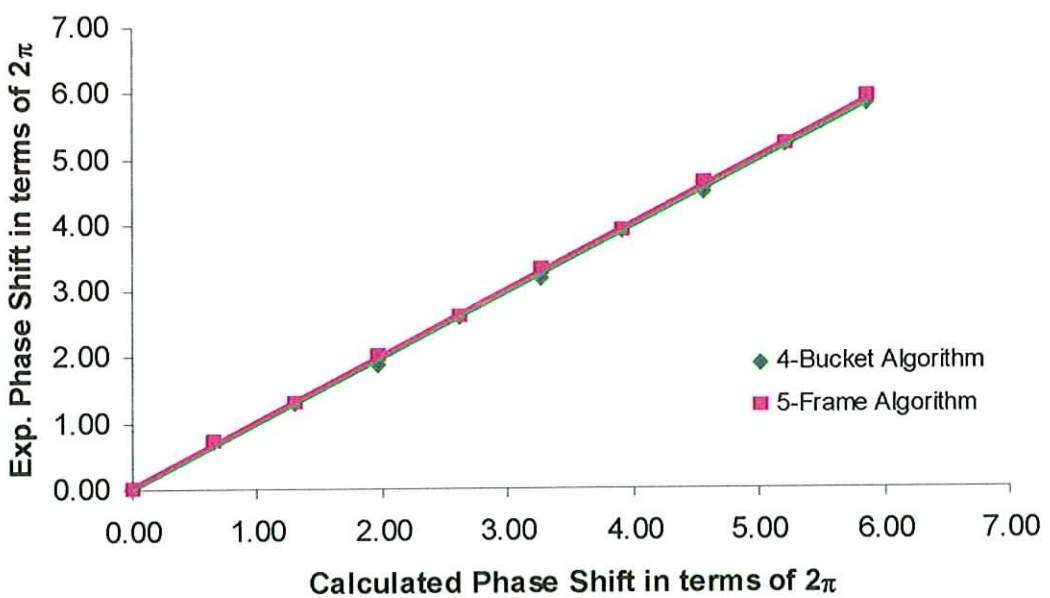

500 frames/sec

2.0μm movement

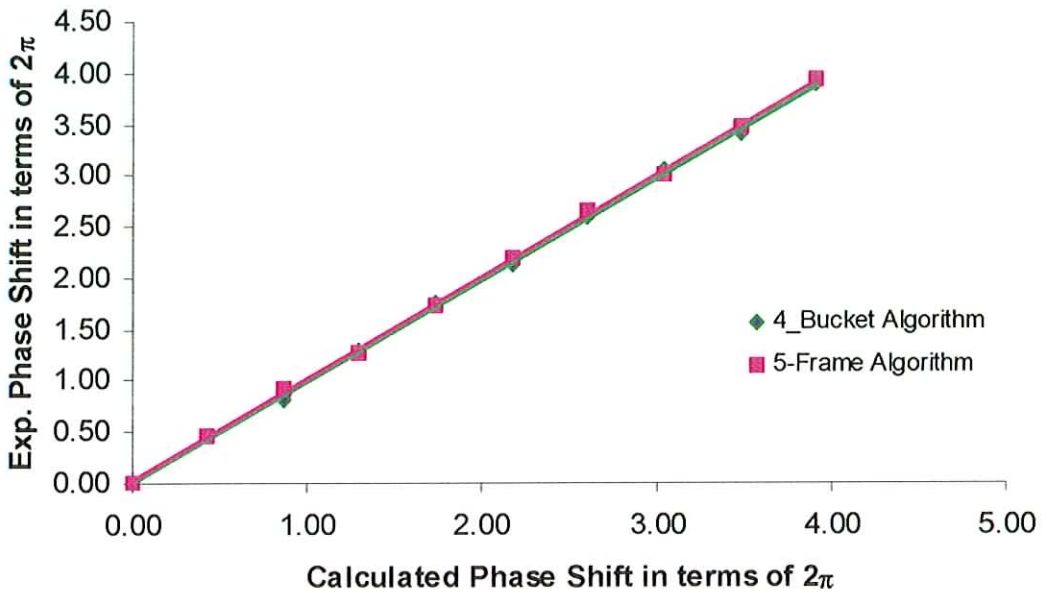

500 frames/sec

5.0μm movement

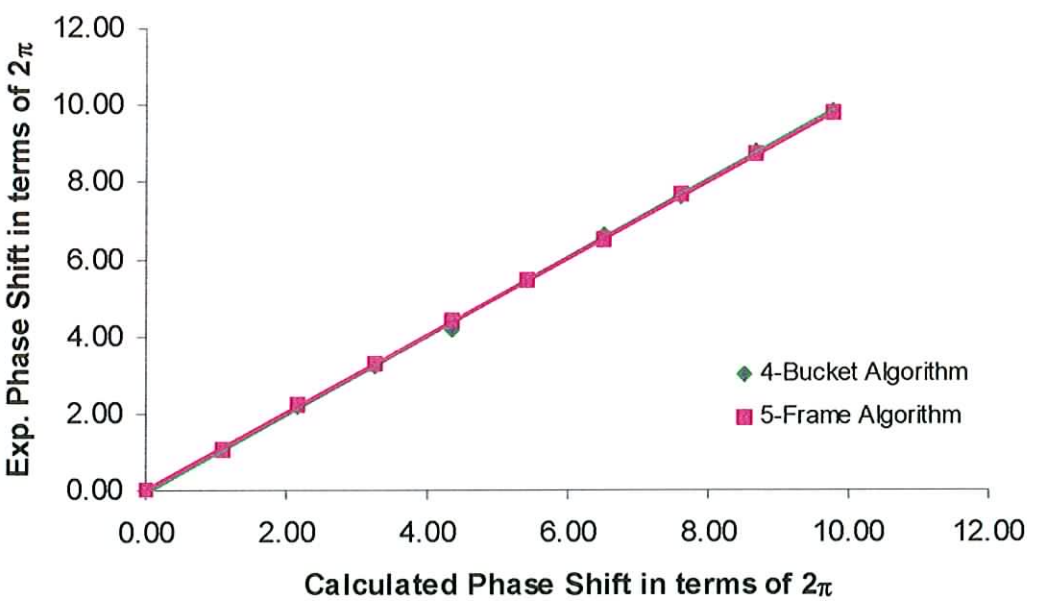

1000 frames/sec

3.0μm movement

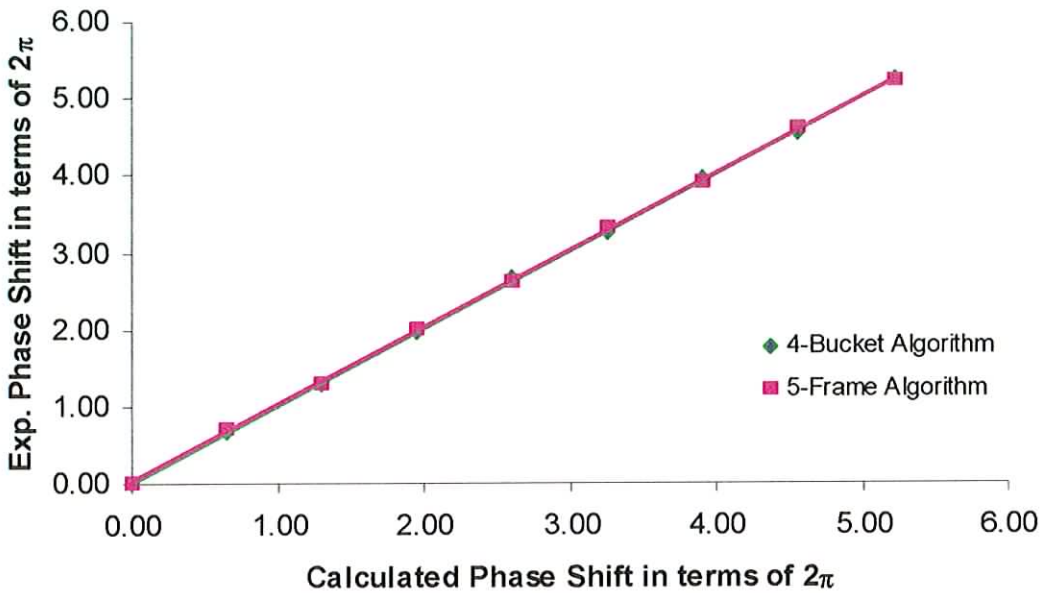

1000 frames/sec

6.0μm movement

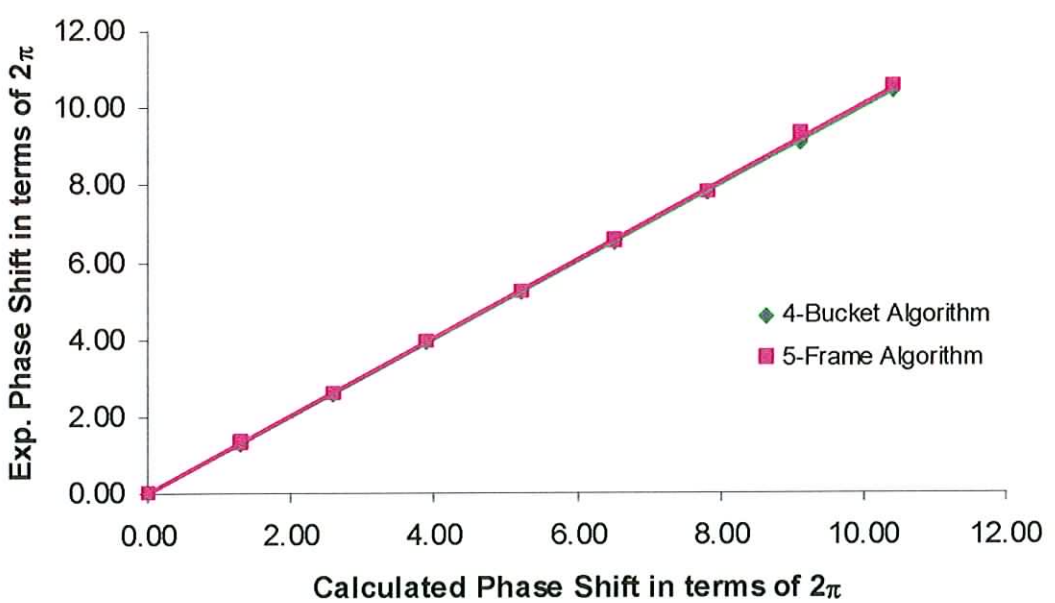

Figure 4.5 Graphs representing the 4-bucket and 5-frame techniques when measuring the same displacement at different speeds

The validity of the 5-frame method can be clearly seen here. The data recorded using this method is comparable with that gathered at a relatively low speed using the 4-bucket algorithm. However, in the case of the 5-frame technique the data was gathered at the high framing rates indicated in table 4.3. These graphs show that the accuracy of the two methods is similar. It is concluded that the 5-frame procedure can record and measure displacements at high speed where the 4-bucket algorithm becomes redundant.

Errors

Table 4.3

Speed when using 5-Frame Algorithm	Displacement on encoder /μm		4-Bucket Algorithm		5-Frame Technique	
			% Error	Standard Deviation	% Error	Standard Deviation
125frames/sec	2.2μm	Exp.	0.97	1.65	0.77	1.63
		Corrected	0.08	1.63	0.38	1.63
	4.0μm	Exp.	0.79	2.45	0.74	2.45
		Corrected	0.33	2.44	0.28	2.45
250 frames/sec	2.0μm	Exp.	1.24	2.32	0.54	2.31
		Corrected	0.75	2.30	0.03	2.31
500frames/sec	2.0μm	Exp.	0.84	4.24	0.21	4.22
		Corrected	0.08	4.22	0.10	4.21
	5.0μm	Exp.	1.93	1.74	0.73	1.74
		Corrected	1.40	1.71	0.15	1.73
1000frames/sec	3.0μm	Exp.	2.64	1.27	1.34	1.28
		Corrected	1.10	1.24	0.38	1.27
	6.0μm	Exp.	1.00	2.92	0.20	2.91
		Corrected	0.96	2.90	0.16	2.90

Table 4.3 shows the percentage errors in each of the trials. It can be seen that, when using the PZT, the faster the frame rate the higher the errors. This is due to the fact that at higher frame rates the full dynamic range of the camera is no longer being used.

It can be seen from these graphs that the 5-frame technique works just as well as the traditional 4-bucket algorithm with even smaller errors and it is therefore concluded that this method can also be used for effective measurement of a displacement.

However, it was important to show that this conclusion holds when measuring the displacement of an uncontrolled object which is moving at high speed.

4.4 Application

The application chosen to demonstrate the use of this method to record the radial expansion of an object was the relaxation of a cylinder. The cylinder was pumped with compressed air by a known amount and thus expanded. It was then allowed to relax and the radial expansion calculated from the following is compared with the radial expansion calculated using the fringe patterns.

$$E = \frac{R_1^2}{(R_2^2 - R_1^2)}(2-\nu)\frac{P}{\varepsilon_t}$$

Equation 4.1

E = modulus of elasticity = 3.3 GN

R_1 = Internal radius of the cylinder = 15.6 cm

R_2 = External radius of the cylinder = 18.6 cm

P = Applied pressure

ν = Poisson's ratio = 0.333

The modulus of elasticity is defined the ratio of stress (force per unit area) to corresponding strain (deformation) in a material under tension or compression.

$$\varepsilon_t = \frac{\Delta R_2}{R_2}, \text{ where } \Delta R_2 = d = \frac{N\lambda}{(1+\cos\theta)}$$

Equation 4.2

θ = Angle between illumination and observation direction = 18.2°

$$\Rightarrow \frac{\Delta R_2}{R_1} = \frac{R_1^{\,2}}{\left(R_2^{\,2} - R_1^{\,2}\right)}(2-\nu)\frac{P}{E}$$

Equation 4.3

This is compared with the calculation using the fringe patterns generated. In the case of out of plane ESPI measurements. When the cylinder is displaced by a distance d the light at the image plane experiences a phase change of $\Delta\phi$ where,

$$\Delta\phi = \frac{4\pi d}{\lambda}$$

Equation 4.4

The difference of phase between two successive bright (or dark) fringes is 2π, therefore the radial expansion that the cylinder undergoes is,

$$d = \frac{\lambda N}{2}$$

λ = Wavelength of light used Equation 4.5

N = Number of fringes

However, there is a small angle θ between the direction of illumination of the object beam and the optical axis of the camera. This affects the phase of the light and the equation becomes

$$\Delta\phi = \frac{2\pi d}{\lambda}(\cos\theta + 1)$$

and Equation 4.6

$$d = \frac{\lambda N}{(1+\cos\theta)}$$

Equation 4.7

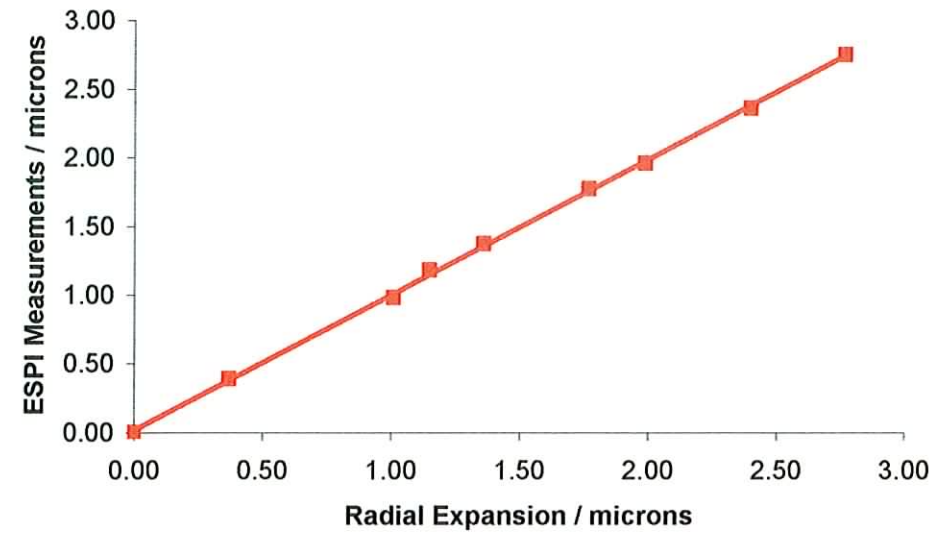

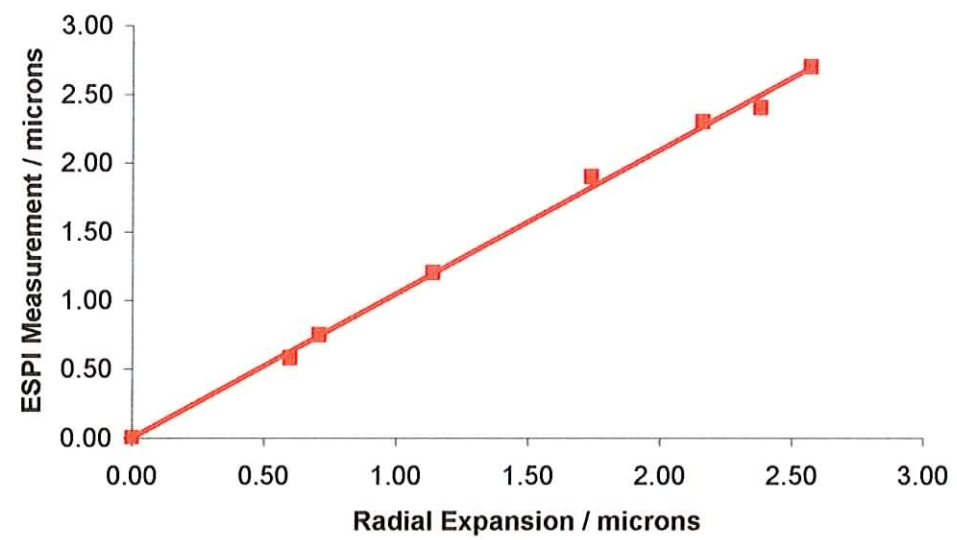

Figure 4.6 Graphs representing the calculation of the radial expansion of the cylinder

It can be seen from the graphs in figure 4.6 that the technique can be used in a real life situation to measure the displacement of a body undergoing a rapid movement. The errors in these graphs are 4.48% and 1.52% respectively, and the standard deviations are 0.93 and 0.87; these errors are well within acceptance. That is, these errors are within $\lambda/100$ which is possible under optimum conditions when using phase maps.

This research was aimed at the design and construction of a system capable of quantitatively observing rapid displacements; an appraisal of the system is as follows:

- The system is compact and mobile
- The data is acquired through the PC allowing for fast digital processing
- Once the system is installed the running costs are negligible
- The distance between the optical head and the PC can be very large, thus allowing for observations in hazardous environments
- The system is not affected by magnetic fields due to the use of the CCD array

CHAPTER 6 REFERENCES

1. Bray D.E., McBride D. "Nondestructive Testing Techniques" Wiley 1992
2. http://www1.faa.gov/avr/afs/300/pdf/2d-ch5_7.pdf, viewed on 1/11/01
3. NASA "Ultrasonic testing of aerospace materials", Practice no. pt-te-1422, pages 4/6, http://www.hq.nasa.gov/office/codeq/relpract/1422msfc.pdf, viewed on 19/01/02
4. Bray D., Stanley R.K., "Nondestructive Evaluation", McGraw-Hill, 1989
5. Erf R.K., "Speckle Metrology", Academic Press, 1978
6. Jones R., Wykes C., "Holographic and Speckle Interferometry", Cambridge Press, 1983
7. http://www.erc.msstate.edu/~foley/newtop/mod_int_the_mic.html, viewed on 26/5/02
8. Robinson D.W., Reid G.T., "Interferogram Analysis", Institute of Physics Publishing Ltd 1993
9. http://wwwfg.rz.uni-karlsruhe.de/~ig59/airbag1998/node2.html, viewed on 17/12/01
10. http://cord.org/cm/leot/course10_Mod04/Module10-4.htm, viewed on 3/10/02
11. http://www.grc.nasa.gov/WWW/OptInstr/phsi.html, viewed on 30/2/03
12. Toal V., Rice H., Meskell C., Armstrong C., Bowe B., "Evaluation of high frequency vibrations using ESPI". SPIE Proceedings, Volume 4876, pages 1054-1063, 2002
13. http://www.asf.alaska.edu/apd/software/tutorial/geos_661_lab/phase_unwrapping.html, viewed on 19/6/02
14. Wyant J. C. "Phase-Shifting Interferometry" http://www.opt-sci.arizona.edu/jcwyant viewed on 12/12/01
15. Ek L., Molin N.E., "Determination of the nodal lines and the amplitude of vibration by speckle interferometry", Optics Communications, Vol. 2 No. 9, Nov. 1970

16. Monaco E., Fontana M., De Rosa L., Bellucci F., Lecce L., "Non-destructive technique based on vibration measurement and piezoelectric patches for monitoring corrosion phenomena", SPIE Proceedings Vol. 4701, pages 78-85, 2002.
17. Reeves M., Taylor N., Edwards C., Williams D., Buckberry C. H., "A study of brake disc modal behaviour during squeal generation using high-speed electronic speckle pattern interferometry and near-field sound pressure measurements" Proc. Instn. Mech. Engrs. Vol. 214 Part D. pages 285 – 296. 2000
18. Buckberry C., Reeves M., Moore A. J., Hand D. P., Barton J. S., Jones J. D. C., "The application of high-speed TV-holography to time-resolved vibration measurements", Optics and Laser Engineering, Volume 32, Issue: 4, pages 387-394. 2000
19. Kilpatrick J. M., Moore A. J., Barton J. S., Jones J. D. C., Reeves M., Buckberry C., "Measurement of complex surface deformation by high-speed dynamic phase-stepped digital speckle pattern interferometry", Optics Letters Vol. 25 No. 15, pages 1068-1070, 2000.
20. Halkon B., Rothberg S., "Comprehensive velocity sensitivity model for scanning and tracking laser vibrometry", SPIE Proceedings Vol. 4827 Paper #: 4827-46, pages 9-21
21. http://www.stiweb.com/appnotes/accel.htm, viewed on 18/8/02
22. Houwing A.P.F, Takayama K., Koremoto K., Hashimoto T., Mitobe H., "Finite fringe Analysis of two dimensional and axially-symmetric flows", Institute of Fluid Science
www.anu.edu.au/Physics/aldir/publications/ Houwing_JSWS_1999.pdf
Viewed on 14/10/03
23. D. Albrecht "Electronic Speckle Pattern Interferometry, Instruments Development, Optimisation and Applications", European Commission Joint Research Centre, Doctoral Thesis, U. of Loughborough, pub. No. I.99.40. 1998
24. ESPItest Software, developed by Andreas Langhoff (http://www.daedalussoft.com) and Maurice Whelan, Copyright © 1998 European Commission, DG - Joint Research Centre, Ispra, Italy.

25. Emilia Mihaylova, Izabela Naydenova, Suzanne Martin, Vincent Toal, "Electronic speckle pattern interferometer with a photopolymer holographic grating", Applied Optics 43 (12), 2439 - 2442, 2004.
26. http://www.coherent.com/Downloads/VerdiV2V5V6_DS_final.pdf
viewed on 26/05/04
27. E. Cadoni, B. Bowe, D. Albrecht, "Application of ESPI technique to evaluate the crack propagation zone of pre-notched clay elements", International Conference on Applied Optical Metrology, Balatonfured, Hungary, June 8-11, 1998.
28. B V Dorr´io and J L Fern´andez, "Phase-evaluation methods in whole-field optical measurement techniques", Meas. Sci. Technol. 10 (1999) R33–R55.
29. E.Mihaylova, B.Potelon, S.Reddy, V.Toal and C.Smith, "Mechanical characterization of unplasticised polyvinyl chloride thick pipes by optical methods", Optics and Lasers in Engineering, 41, 889-900, 2004.

Appendix 1

Software

Section of Program which Creates and Saves Five "Ideal" Fringe Patterns

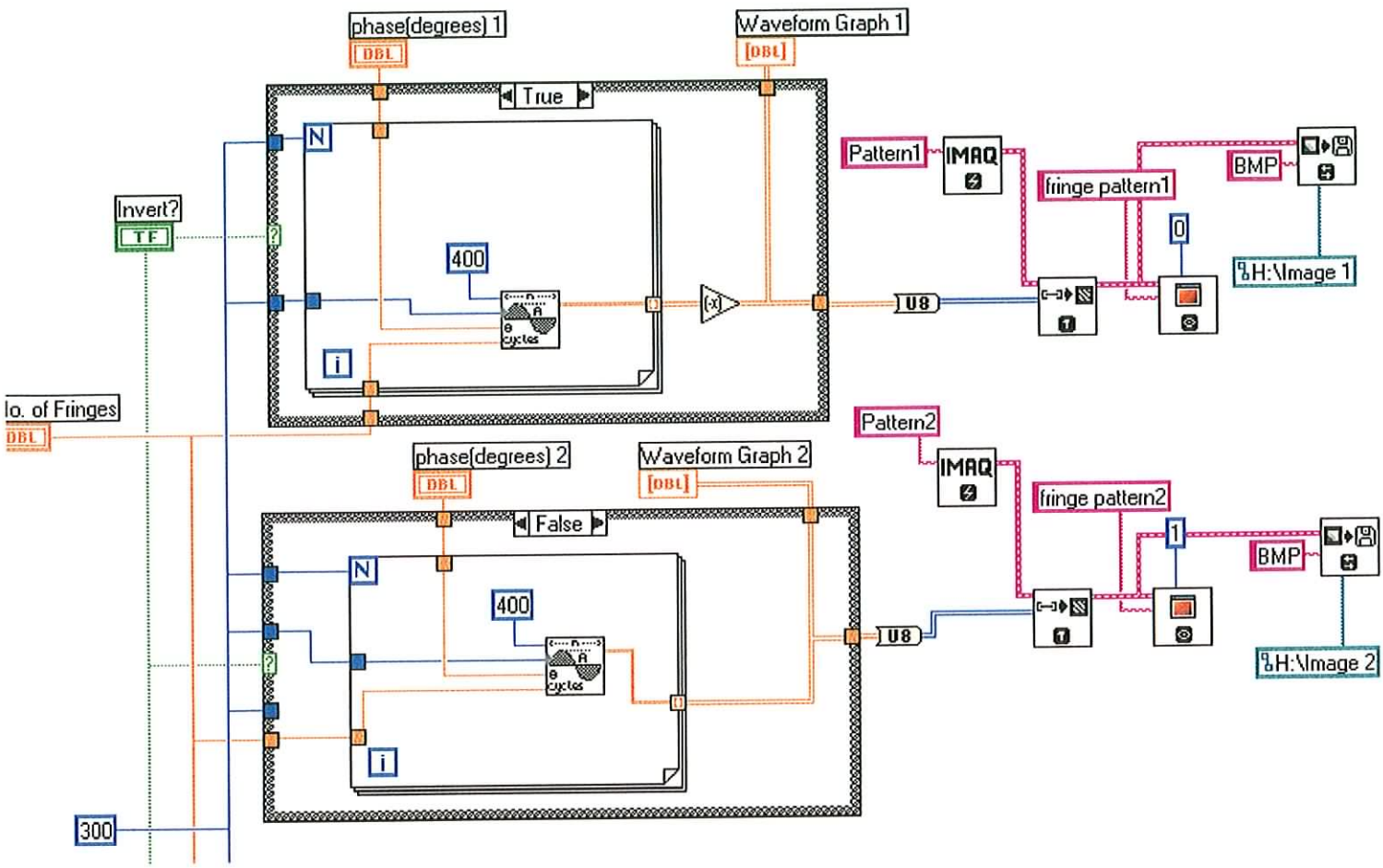

Section of LabVIEW Program which Implements the 4-Bucket Algorithm

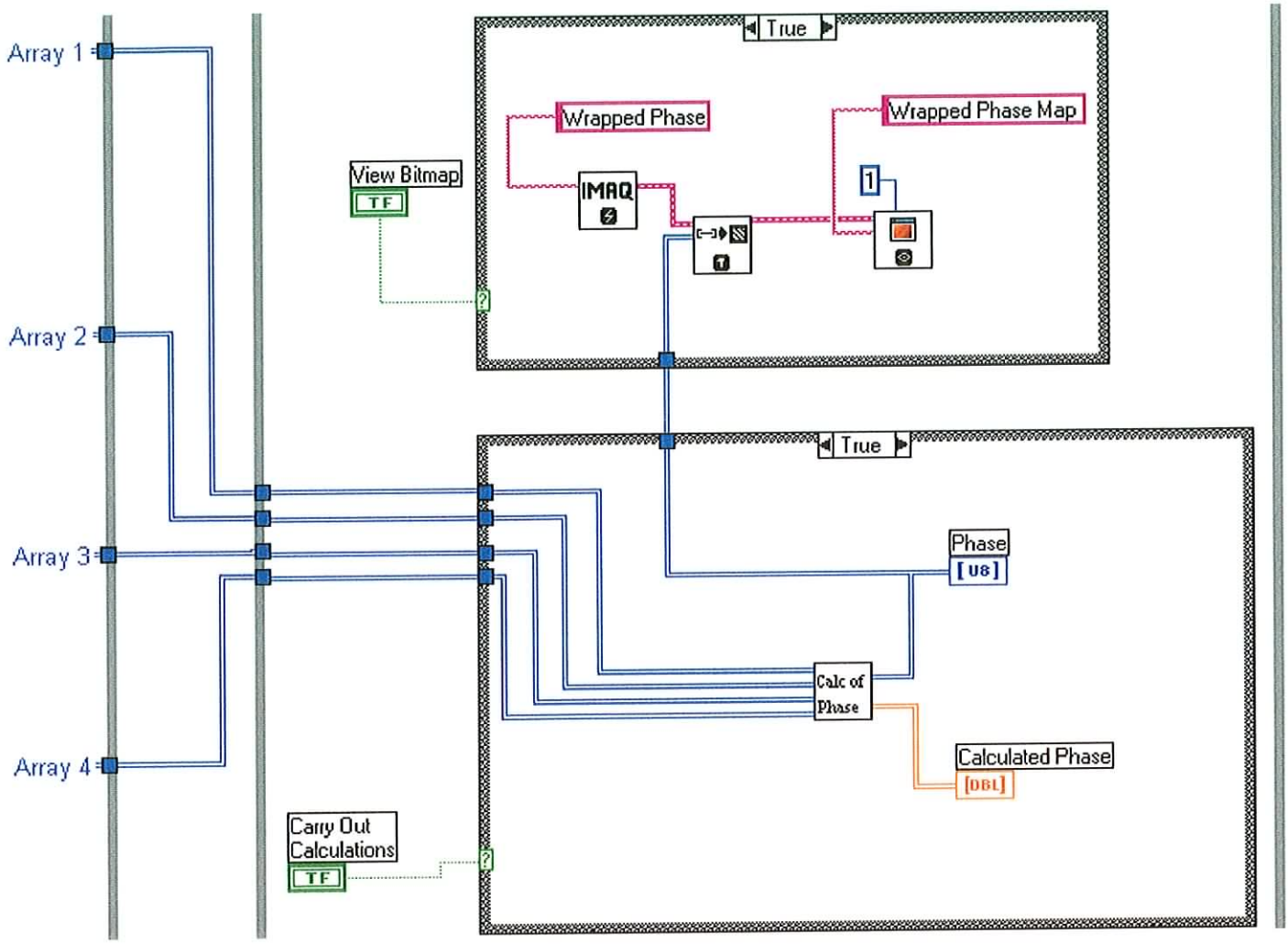

Section of LabVIEW Program, which Implements the 5-Image Algorithm

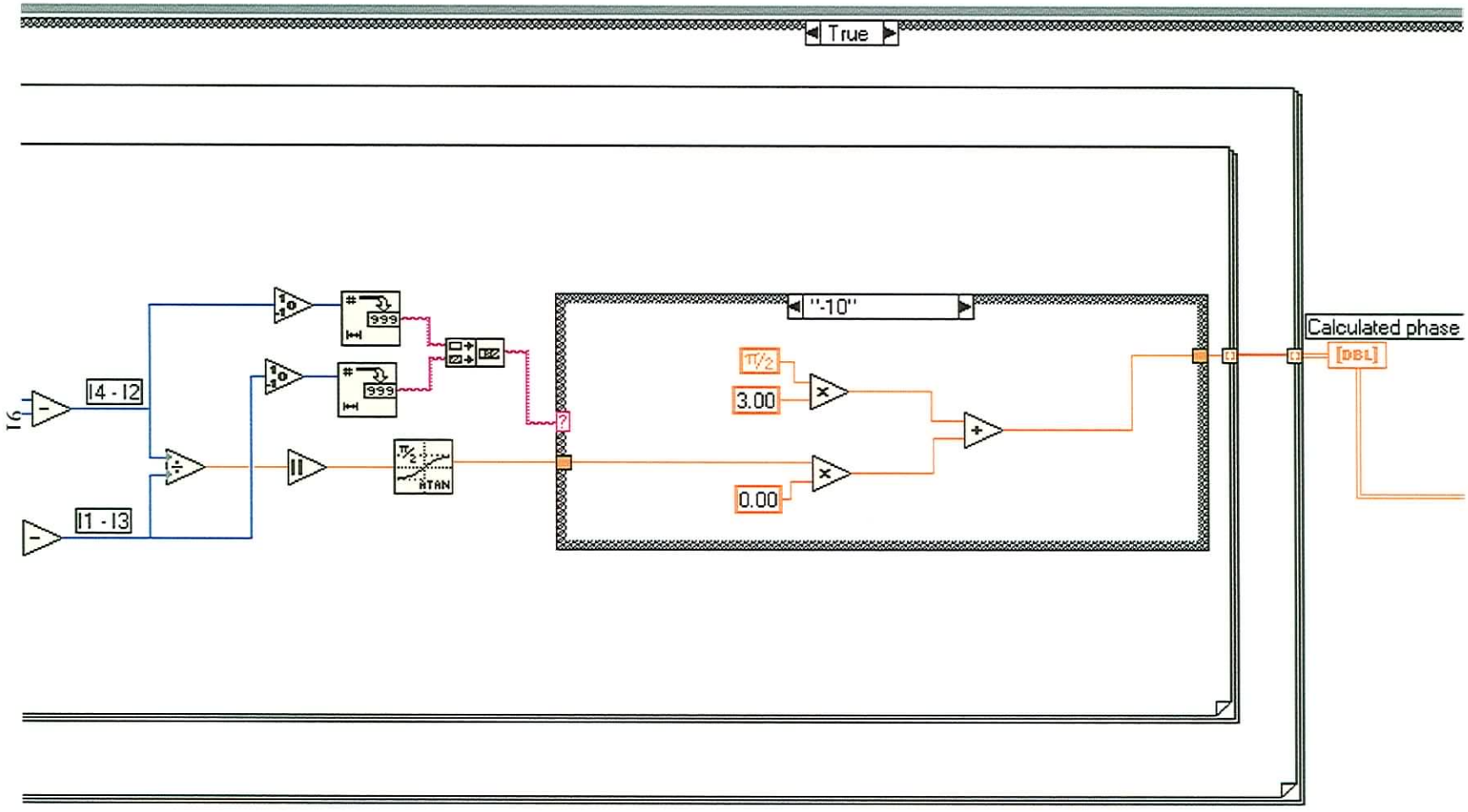

Since the phase is calculated from an arctan there are discontinuities in the phase calculation. Usually the arctan is defined over a range of $-\pi/2$ to $+\pi/2$. However in phase-shifting interferometry the signs of the individual sines and cosines are known. This means that we know which quadrant the phase is in, so when the arctan is performed the phase is determined over a range of $-\pi$ to $+\pi$.

The case structure looks at how the phase is determined by examining the signs of these quantities after the phase is calculated.

Block Diagram of VI which Calculates δ from the Previous Two Programs

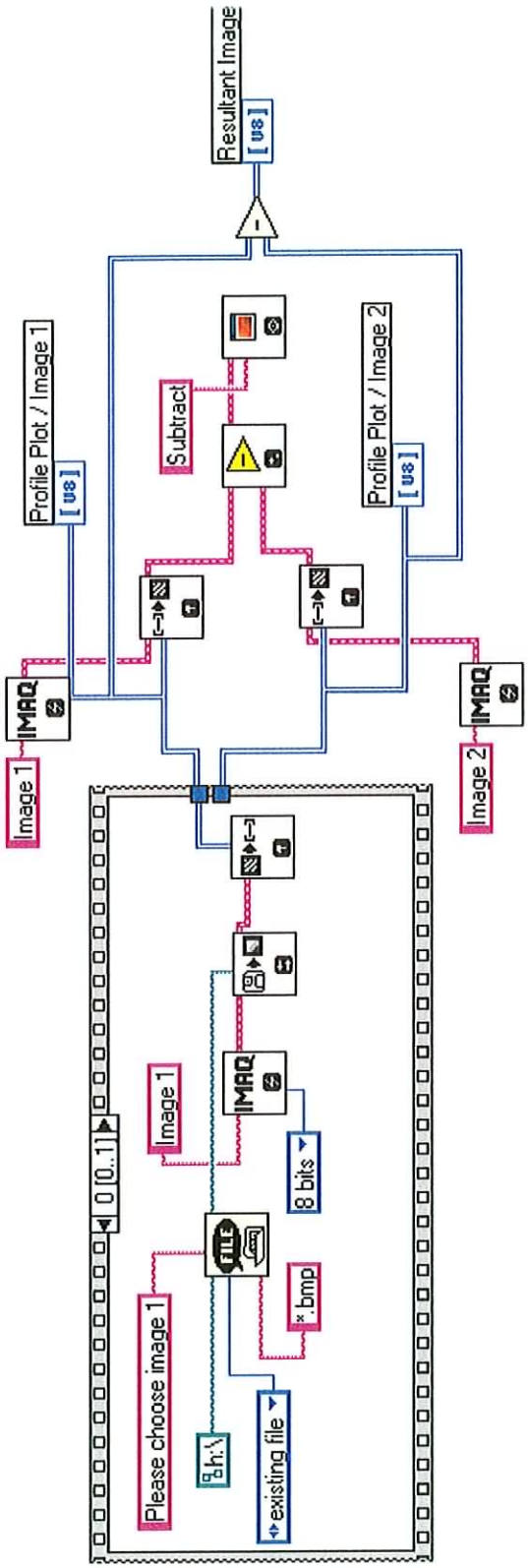

Section of Program which Calibrates the PZT

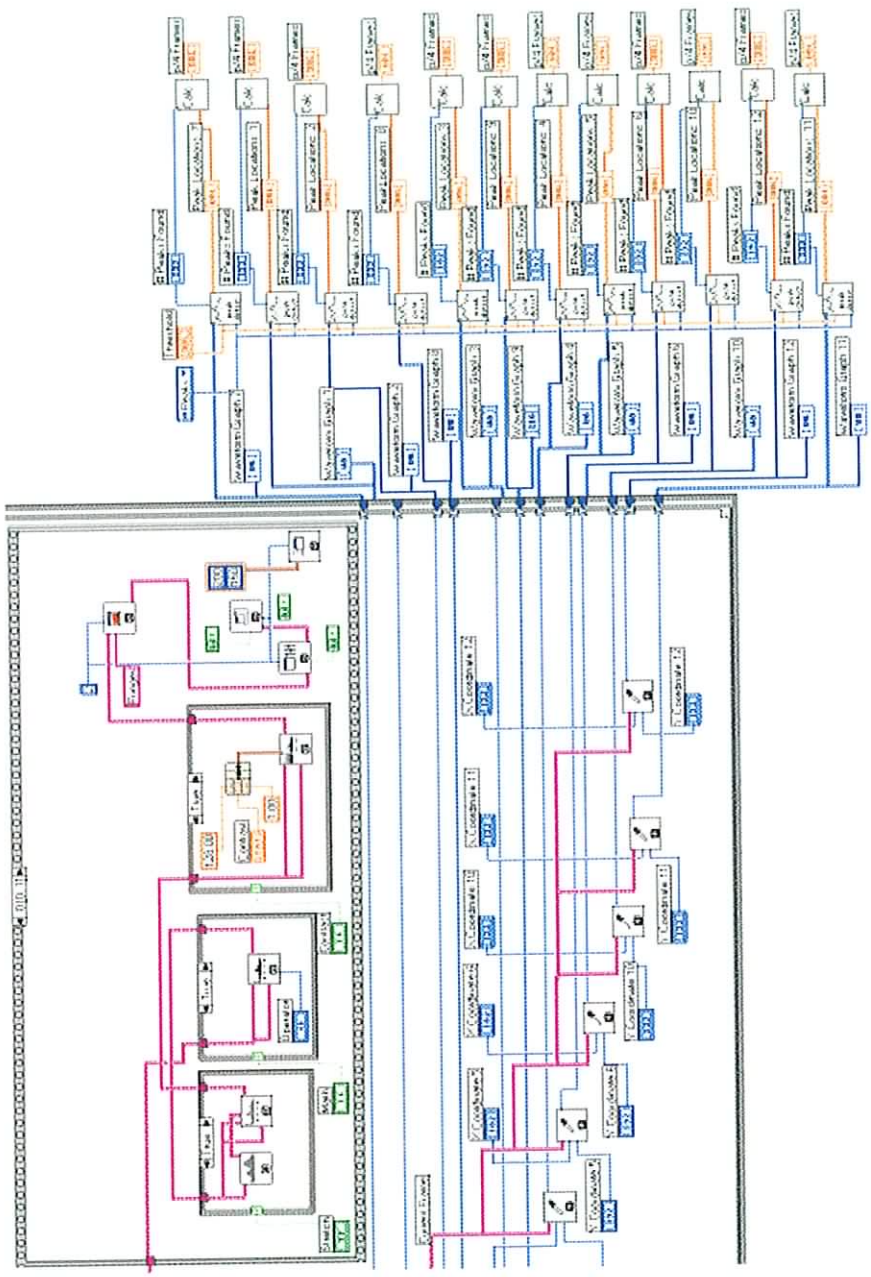

Appendix 2

Data

Data recorded when calibrating the system using conventional ESPI

Displacements Calculated From Rotational Stage / μm	ESPI Illumination angle = 19.5^0 as measured from centre of disc	Corrected Illumination angle = 19.9^0
0.00	0.00	0.00
1.62	1.65	1.62
3.26	3.29	3.23
4.89	4.94	4.85
6.51	6.70	6.58
8.14	8.35	8.20
9.77	9.99	9.82
11.40	11.64	11.43
13.03	13.29	13.05
14.66	14.93	14.67
15.74	15.87	15.59

Table A2-1 Data recorded from calibration with conventional camera

Data recorded when calibrating the system using high-speed ESPI

Camera capturing images at a rate of 125 frames/s

The encoder has a linear velocity of 10μm/s which corresponds to an angular velocity of the disc of 6.22×10^{-2} degrees per second.

Displacements Calculated From Rotational Stage / μm	Calculated Displacement using ESPI/μm	Corrected for error in θ /μm
0.00	0.00	0.00
3.00	2.77	2.90
4.00	3.77	3.96
5.00	4.76	4.99
6.00	5.80	6.08
7.00	6.68	7.00
8.00	7.84	8.22
9.00	8.63	9.04

Table A2-2 High Speed camera capturing images at a rate of 125 frames/s

Camera capturing images at a rate of 125 frames/s

Encoder linear velocity of 15μm/s, angular velocity 9.33×10^{-2} degrees per second

Displacements Calculated From Rotational Stage / μm	Calculated Displacement using ESPI/μm	Corrected for error in θ /μm
0.00	0.00	0.00
4.50	4.17	4.37
6.00	5.29	5.54
7.50	6.84	7.17
9.00	8.21	8.61
10.50	9.92	10.40
12.00	11.17	11.70
13.50	12.61	13.21

Table A2-3 High Speed camera capturing images at a rate of 125 frames/s

Camera capturing images at a rate of 250 frames/s

Encoder linear velocity of 40μm/s, angular velocity 24.88×10^{-2} degrees per second

Displacements Calculated From Rotational Stage / μm	Calculated Displacement using ESPI/μm	Corrected for error in θ /μm
0.00	0.00	0.00
6.00	5.74	6.18
8.00	7.93	7.59
10.00	9.34	10.06
12.00	11.15	12.00
14.00	13.41	14.44
16.00	15.60	15.87
18.00	17.50	17.81

Table A2-4 High Speed camera capturing images at a rate of 250 frames/s

Camera capturing images at a rate of 1000 frames/s

Encoder linear velocity of 30μm/s, angular velocity 18.66×10^{-2} degrees per second

Displacements Calculated From Rotational Stage / μm	Calculated Displacement using ESPI/μm	Corrected for error in θ /μm
0.00	0.00	0.00
3.00	2.75	2.99
3.37	3.18	3.46
3.75	3.56	3.87
4.12	3.66	3.99
4.50	4.03	4.38
4.87	4.47	4.87
5.25	4.78	5.20

Table A2-5 High Speed camera capturing images at a rate of 1000 frames/s

Camera capturing images at a rate of 1000 frames/s

Encoder linear velocity of 40μm/s, angular velocity 24.88×10^{-2} degrees per second

Displacements Calculated From Rotational Stage / μm	Calculated Displacement using ESPI/μm	Corrected for error in θ /μm
0.00	0.00	0.00
6.00	5.76	6.09
8.00	7.49	7.90
10.00	9.35	9.87
12.00	11.20	11.83
14.00	13.38	14.12
16.00	15.66	15.53
18.00	17.50	17.45

Table A2-6 High Speed camera capturing images at a rate of 1000 frames/s

Camera capturing images at a rate of 1000 frames/s

Encoder linear velocity of 45μm/s, angular velocity 27.99×10^{-2} degrees per second

Displacements Calculated From Rotational Stage / μm	Calculated Displacement using ESPI/μm	Corrected for error in θ /μm
0.00	0.00	0.00
2.81	2.68	2.90
3.37	2.94	3.18
3.94	3.54	3.82
4.50	4.12	4.46
5.06	4.76	5.15
5.62	5.16	5.58
6.19	5.99	6.48

Table A2-7 High Speed camera capturing images at a rate of 1000 frames/s

Data recorded when calibrating the system using Phase-Shifting ESPI

d/μm	Δϕ Experimental	Δϕ Corrected for θ
0.00	0.00	0.00
1.63	1.59	1.64
2.44	2.36	2.42
3.26	3.21	3.29
4.89	4.76	4.81
5.70	5.65	5.72
6.51	6.40	6.55
7.33	7.27	7.31
8.14	8.18	8.20
8.96	8.99	9.02
9.77	9.66	9.72

Table A2-8 Calibration by Phase Shifting ESPI

d/μm	Δϕ Experimental	Δϕ Corrected for θ
0.00	0.00	0.00
5.70	5.64	5.72
6.51	6.46	6.57
7.33	7.29	7.32
8.14	8.17	8.20
8.96	9.00	9.02
9.77	9.71	9.75
10.58	10.55	10.60
11.39	11.34	11.41
12.20	12.17	12.21
13.01	12.97	13.01
13.82	13.77	13.83

Table A2-9 Calibration by Phase Shifting ESPI

Data Recorded When Calibrating the PZT

Displacement in the x direction/ μm	Calculated Displacement in the x direction/ μm
0.00	0.00
3.00	2.90
6.00	5.71
9.00	8.58
12.00	11.94
15.00	14.93
18.00	17.93
21.00	20.92
24.00	23.88
27.00	26.85

Table A2-10 PZT Calibration data

Data recorded when using phase-shifting ESPI with (a) the 4-bucket algorithm and (b) the 5-frame technique

(a) 4-Bucket Algorithm

Displacements Calculated From Rotational Stage / μm	Calculated Displacement using ESPI/μm	Corrected for error in θ /μm
0.00	0.00	0.00
0.73	0.74	0.74
1.43	1.48	1.48
2.15	2.09	2.10
2.87	2.83	2.84
3.59	3.56	3.58
4.30	4.30	4.32
5.02	4.92	4.94
5.74	5.65	5.68
6.46	6.39	6.42
7.17	7.13	7.16

Table A2-11 Data from 4-Bucket algorithm

Displacements Calculated From Rotational Stage / μm	Calculated Displacement using ESPI/μm	Corrected for error in θ /μm
0.00	0.00	0.00
1.30	1.35	1.36
2.61	2.58	2.59
3.91	3.93	3.94
5.22	5.12	5.17
6.52	6.52	6.53
7.83	7.87	7.88
9.13	9.10	9.12
10.43	10.45	10.47
11.74	11.68	11.70
13.04	13.03	13.05

Table A2-12 Data from 4-Bucket algorithm

Displacements Calculated From Rotational Stage / μm	Calculated Displacement using ESPI/μm	Corrected for error in θ /μm
0.00	0.00	0.00
0.65	0.71	0.71
1.30	1.29	1.30
1.96	1.88	1.89
2.61	2.59	2.60
3.26	3.17	3.19
3.91	3.88	3.90
4.56	4.47	4.49
5.22	5.17	5.20
5.87	5.76	5.79

Table A2-13 Data from 4-Bucket algorithm

Displacements Calculated From Rotational Stage / μm	Calculated Displacement using ESPI/μm	Corrected for error in θ /μm
0.00	0.00	0.00
0.43	0.46	0.47
0.87	0.81	0.82
1.30	1.27	1.29
1.74	1.74	1.76
2.17	2.08	2.12
2.61	2.55	2.59
3.04	3.01	3.06
3.48	3.36	3.41

Table A2-14 Data from 4-Bucket algorithm

Displacements Calculated From Rotational Stage / μm	Calculated Displacement using ESPI/μm	Corrected for error in θ /μm
0.00	0.00	0.00
1.09	1.04	1.04
2.17	2.20	2.19
3.26	3.24	3.24
4.35	4.17	4.16
5.43	5.44	5.43
6.52	6.48	6.59
7.61	7.61	7.63
8.69	8.79	8.78
9.78	9.84	9.82

Table A2-15 Data from 4-Bucket algorithm

Displacements Calculated From Rotational Stage / μm	Calculated Displacement using ESPI/μm	Corrected for error in θ /μm
0.00	0.00	0.00
0.65	0.71	0.68
1.30	1.29	1.28
1.96	2.00	1.97
2.61	2.71	2.67
3.26	3.29	3.26
3.91	4.00	3.95
4.56	4.59	4.53
5.22	5.29	5.23

Table A2-16 Data from 4-Bucket algorithm

Displacements Calculated From Rotational Stage / μm	Calculated Displacement using ESPI/μm	Corrected for error in θ /μm
0.00	0.00	0.00
1.30	1.29	1.30
2.61	2.59	2.60
3.91	3.88	3.90
5.22	5.18	5.20
6.52	6.47	6.50
7.83	7.76	7.80
9.13	9.06	9.10
10.43	10.35	10.40

Table A2-17 Data from 4-Bucket algorithm

(b) 5-Frame Algorithm

Displacements Calculated From Rotational Stage / μm	Calculated Displacement using ESPI/μm	Corrected for error in θ /μm
0.00	0.00	0.00
0.72	0.74	0.73
1.43	1.45	1.47
2.15	2.21	2.20
2.87	2.83	2.82
3.59	3.56	3.55
4.30	4.30	4.28
5.02	5.04	5.02
5.74	5.78	5.75
6.46	6.52	6.49
7.17	7.13	7.10

Table A2-18 Data from 5-Frame algorithm capturing frames at a rate of 125 frames/sec

Displacements Calculated From Rotational Stage / μm	Calculated Displacement using ESPI/μm	Corrected for error in θ /μm
0.00	0.00	0.00
1.30	1.35	1.34
2.61	2.58	2.56
3.91	3.93	3.90
5.22	5.29	5.24
6.52	6.64	6.58
7.83	7.87	7.81
9.13	9.22	9.15
10.43	10.57	10.49
11.74	11.80	11.71
13.04	13.15	13.05

Table A2-19 Data from 5-Frame algorithm capturing frames at a rate of 125 frames/sec

Displacements Calculated From Rotational Stage / μm	Calculated Displacement using ESPI/μm	Corrected for error in θ /μm
0.00	0.00	0.00
0.65	0.71	0.71
1.30	1.29	1.30
1.96	2.00	2.01
2.61	2.59	2.60
3.26	3.29	3.31
3.91	3.88	3.90
4.56	4.58	4.61
5.22	5.17	5.20
5.87	5.87	5.90

Table A2-20 Data from 5-Frame algorithm capturing frames at a rate of 250 frames/sec

Displacements Calculated From Rotational Stage / μm	Calculated Displacement using ESPI/μm	Corrected for error in θ /μm
0.00	0.00	0.00
0.43	0.46	0.46
0.87	0.93	0.93
1.30	1.27	1.27
1.74	1.74	1.73
2.17	2.20	2.20
2.61	2.66	2.66
3.04	3.01	3.01
3.48	3.36	3.47
3.91	3.94	3.93

Table A2-21 Data from 5-Frame algorithm capturing frames at a rate of 500 frames/sec

Displacements Calculated From Rotational Stage / μm	Calculated Displacement using ESPI/μm	Corrected for error in θ /μm
0.00	0.00	0.00
1.09	1.04	1.05
2.17	2.20	2.21
3.26	3.24	3.25
4.35	4.40	4.41
5.43	5.44	5.46
6.52	6.48	6.50
7.61	7.64	7.67
8.69	8.68	8.71
9.78	9.72	9.76

Table A2-22 Data from 5-Frame algorithm capturing frames at a rate of 500 frames/sec

Displacements Calculated From Rotational Stage / μm	Calculated Displacement using ESPI/μm	Corrected for error in θ /μm
0.00	0.00	0.00
0.65	0.71	0.71
1.30	1.29	1.30
1.96	2.00	2.00
2.61	2.59	2.60
3.26	3.29	3.31
3.91	3.88	3.90
4.56	4.59	4.60
5.22	5.18	5.20

Table A2-22 Data from 5-Frame algorithm capturing frames at a rate of 1000 frames/sec

Displacements Calculated From Rotational Stage / μm	Calculated Displacement using ESPI/μm	Corrected for error in θ /μm
0.00	0.00	0.00
1.30	1.29	1.30
2.61	2.59	2.60
3.91	3.88	3.90
5.22	5.18	5.20
6.52	6.47	6.50
7.83	7.76	7.80
9.13	9.18	9.22
10.43	10.47	10.52

Table A2-23 Data from 5-Frame algorithm capturing frames at a rate of 1000 frames/sec

Data recorded when using phase-shifting ESPI with the 5-frame technique on an industrial application

Elongation/μm	N/fringes	d/ μm
0.00	0.0	0.00
0.60	1.5	0.58
0.71	2.0	0.75
1.14	3.0	1.20
1.74	4.5	1.90
2.16	5.5	2.30
2.38	6.0	2.40
2.57	7.0	2.70

Table A2-24 Data from 5-Frame algorithm on an industrial application

Elongation/μm	N/fringes	d/ μm
0.00	0.0	0.00
0.37	1.0	0.39
1.01	2.5	0.98
1.15	3.0	1.18
1.36	3.5	1.37
1.77	4.5	1.77
1.99	5.0	1.96
2.40	6.0	2.36
2.77	7.0	2.75

Table A2-25 Data from 5-Frame algorithm on an industrial application

Appendix 3

Equipment Specs

Frequency Doubled Yttrium Vanadate Laser[26]

System Specifications

Wavelength	532 nm
Linewidth	<5 MHz
Beam Diameter	2.25 mm ±10%
Beam Divergence	<0.5 mrad
Pointing Stability	<2 μrad/°C
Power Stability	±1%
Noise	<0.03% rms
Polarization vertical,	>100:1

Utility and Environmental Requirements

Operating Voltage	100 to 240 VAC
Operating Current	13A max.@ 100 VAC
Power Consumption	1.3 kW maximum 300W typical
Frequency	50 to 60 Hz
Laser Head Cooling Requirements	Conductivity-cooled (or optional heat sink, with or without a closed-cycle chiller)
Power Supply Cooling Requirements	Air-cooled
Range of Operating Temperature	15°C to 35°C
Weights Laser Head Power Supply	 10 kg (22.0 lbs.) 31.5 kg (69.4 lbs.)